AGU ADVANCING EARTH AND SPACE SCIENCES

Earth and Space Science

RESEARCH ARTICLE
10.1029/2026EA005247

Robust Regional Contrast but Penetration-Sensitive Snow Thickness Over Sea Ice From Multi-Winter Antarctic CRYO2ICE Observations

Xinlong Liu[1,2,3], Alexander D. Fraser[1,2], Rachel L. Tilling[4,5], Petra Heil[2,6], and Stuart P. Corney[1,2]

[1]Institute for Marine and Antarctic Studies, University of Tasmania, Hobart, TAS, Australia, [2]Australian Antarctic Program Partnership, Institute for Marine and Antarctic Studies, University of Tasmania, Hobart, TAS, Australia, [3]Now at the Institute for Marine and Antarctic Studies, University of Tasmania, Battery Point, TAS, Australia, [4]Cryospheric Sciences Laboratory, NASA Goddard Space Flight Center, Greenbelt, MD, USA, [5]Earth System Science Interdisciplinary Center, University of Maryland, College Park, MD, USA, [6]British Antarctic Survey, Cambridge, UK

Key Points:

- Weddell Sea snow is thicker than Ross Sea snow under common dual-altimetry retrieval assumptions across four sampled winters
- Formal per-matchup precision is approximately 0.04 m and dominated by CryoSat-2 radar freeboard rather than snow density assumptions
- AMSR2 reproduces the regional ordering but explains little retrieval-scale CRYO2ICE variability

Correspondence to:

X. Liu,
xinlong.liu@utas.edu.au

Citation:

Liu, X., Fraser, A. D., Tilling, R. L., Heil, P., & Corney, S. P. (2026). Robust regional contrast but penetration-sensitive snow thickness over sea ice from multi-winter Antarctic CRYO2ICE observations. *Earth and Space Science*, *13*, e2026EA005247. https://doi.org/10.1029/2026EA005247

Received 27 APR 2026
Accepted 29 JUL 2026

Author Contributions:

Conceptualization: Xinlong Liu, Rachel L. Tilling, Petra Heil
Data curation: Xinlong Liu, Rachel L. Tilling
Formal analysis: Xinlong Liu, Alexander D. Fraser, Rachel L. Tilling, Petra Heil, Stuart P. Corney
Funding acquisition: Xinlong Liu
Investigation: Xinlong Liu, Alexander D. Fraser, Stuart P. Corney
Methodology: Xinlong Liu, Alexander D. Fraser, Rachel L. Tilling, Stuart P. Corney
Project administration: Xinlong Liu, Alexander D. Fraser, Petra Heil, Stuart P. Corney
Resources: Xinlong Liu, Rachel L. Tilling
Software: Xinlong Liu
Supervision: Xinlong Liu, Petra Heil

Abstract

Snow on Antarctic sea ice modulates albedo, thermodynamic growth, and snow–ice formation, yet remains a leading uncertainty in altimetry-derived sea-ice thickness. Here we use the post-2022 CRYO2ICE configuration to derive along-track winter snow thickness from ICESat-2 laser and CryoSat-2 Ku-band radar freeboards over the Weddell and Ross sectors. We analyze 82,341 winter matchups (August 2022–September 2025) using a 5 km, 4 hr collocation criterion and propagate freeboard and snow-density uncertainties. Retrieved snow thickness is consistently larger in the Weddell Sea (mean 0.255 m, median 0.188 m) than the Ross Sea (0.217 m, 0.156 m), consistent with the older, thicker western Weddell ice. The contrast persists across sampled months and years and under common snow-density and penetration-factor assumptions. Formal per-matchup precision (0.039–0.040 m) is dominated by CryoSat-2 radar-freeboard uncertainty, whereas the absolute magnitude is set by the unresolved Ku-band scattering horizon. Comparison with AMSR2 passive-microwave snow depth shows weak point-to-point agreement ($r^2 = 0.062$ and <0.001 in the Weddell and Ross sectors), reflecting differing measurement physics and spatial support. Nevertheless, both independently reproduce thicker Weddell than Ross snow. Under a common penetration factor, absolute sector-mean snow thickness varies by approximately a factor of two across the tested range, whereas the sector ordering is preserved under any uniform choice of penetration factor. CRYO2ICE therefore resolves a repeatable regional freeboard-difference signal, but conversion of that signal to absolute snow thickness remains conditional on the poorly constrained, ice-regime-dependent Ku-band scattering horizon.

Plain Language Summary

Snow on Antarctic sea ice plays a central role in the polar climate system. It reflects sunlight back to space, insulates the underlying ice from the cold winter atmosphere, and adds weight that can push the ice below the waterline. Despite this importance, the thickness of snow on Antarctic sea ice is one of the least well-measured quantities in the polar regions. We combine two satellites that respond to different effective surfaces within the snow–ice system: ICESat-2 measures near the snow surface, whereas CryoSat-2 responds to a Ku-band scattering horizon that can lie within the snowpack or near the snow–ice interface. Across four austral winters between 2022 and 2025, we analyze 82,341 near-coincident measurement pairs over the Weddell and Ross Sea sectors. Our results show that snow on Weddell Sea sea ice is consistently thicker than snow on Ross Sea sea ice, by about four centimetres on average. An independent passive-microwave snow-depth product confirms the same regional pattern. These findings provide a baseline against which the upcoming European Copernicus CRISTAL mission can be evaluated, helping to improve future estimates of how much snow lies on Antarctic sea ice.

1. Introduction

Antarctic sea ice is a critical component of the global climate system, governing Southern Ocean albedo, air–sea heat and gas exchange, deep water formation, and ecosystem productivity (Parkinson, 2019; Parkinson & DiGirolamo, 2021; Turner et al., 2017). Snow deposited at the upper sea-ice surface plays a disproportionate role through multiple pathways: its high albedo amplifies the ice-albedo feedback (Liston et al., 2018), while its low thermal conductivity insulates the underlying ice from the cooler winter atmosphere, strongly modulating thermodynamic growth in autumn and winter and melt rates in spring and summer (Moon et al., 2019; Webster

Validation: Xinlong Liu, Rachel L. Tilling, Petra Heil
Visualization: Xinlong Liu, Rachel L. Tilling
Writing – original draft: Xinlong Liu
Writing – review & editing: Xinlong Liu, Alexander D. Fraser, Rachel L. Tilling, Petra Heil, Stuart P. Corney

et al., 2018). Snow loading may also depress the upper sea-ice surface below the waterline, enabling seawater flooding and, under freezing conditions, snow–ice formation (Arndt et al., 2021, 2024, 2025), a process that contributes substantially to the total sea-ice mass budget in Antarctica (Massom et al., 2001; Sturm & Massom, 2017). Accurate knowledge of snow thickness on Antarctic sea ice is therefore essential for constraining each of these processes, and is the single largest source of uncertainty in satellite radar altimetric retrievals of sea-ice thickness (Arndt et al., 2024, 2025; Kwok et al., 2020), because both the mass loading on the ice and the reduced radar propagation speed through the snowpack must be accurately known to convert freeboard to thickness (Fredensborg Hansen et al., 2024, 2025b; Giles et al., 2008).

Despite its importance, the thickness of snow on Antarctic sea ice remains poorly constrained at large scales. The most comprehensive in situ compilation, the Antarctic Sea Ice Processes and Climate (ASPeCt) ship-based data set of Worby, Geiger, et al. (2008), is spatially limited and seasonally biased. Its observations are representative only of snow on level ice because the protocol does not correct for thicker snow over deformed surfaces (Worby, Markus, et al., 2008), and ship-based sampling is further biased because vessels preferentially navigate through thinner, less deformed ice (Williams et al., 2015). The longest satellite-derived snow-depth record comes from the passive-microwave Advanced Microwave Scanning Radiometer instruments (Advanced Microwave Scanning Radiometer - Earth Observing System (AMSR-E) and its successor AMSR2). These exploit the frequency-dependent scattering of microwave radiation by snow grains to estimate snow depth from the brightness-temperature gradient between the 19 and 37 GHz channels (Markus & Cavalieri, 1998; Meier et al., 2018). This approach provides daily circumpolar coverage at 12.5–25 km resolution, but the retrieval is limited to dry snow, with retrieval skill degrading above approximately 0.30 m and an effective ceiling near 0.50 m (Markus & Cavalieri, 1998; Rostosky et al., 2018). Its accuracy further degrades over deformed and multi-year ice (MYI) where surface roughness alters the effective emissivity (Worby, Markus, et al., 2008; S. Kern & Ozsoy-Çiçek, 2016; Rostosky et al., 2018). Worby, Markus, et al. (2008) showed that AMSR-E underestimates snow depth by a factor of 2.3 relative to in situ measurements over rough East Antarctic sea ice, while S. Kern and Ozsoy-Çiçek (2016) found substantial inter-algorithm spread among empirical passive-microwave approaches applied to the Southern Ocean.

A complementary spaceborne approach derives snow thickness from the difference between surface elevations measured by two co-located altimeters: a laser altimeter, which reflects from near the air–snow interface, and a Ku-band radar altimeter, which penetrates toward the snow–ice interface (Guerreiro et al., 2016; Kacimi & Kwok, 2020; Kwok et al., 2020; Nab et al., 2024). This laser–Ku-band (LaKu) concept was first demonstrated in the Arctic using gridded ICESat-2 (IS2) and CryoSat-2 (CS2) freeboards (Fredensborg Hansen et al., 2024; Kacimi & Kwok, 2022; Kwok et al., 2020), and Kacimi and Kwok (2020) extended it to the Antarctic by producing the first circumpolar snow-thickness maps from gridded IS2–CS2 freeboard differences for a single year (April–November 2019). The CRYO2ICE (C2I) satellite configuration (Saha et al., 2025) realises the LaKu concept along-track at spaceborne scales: in July 2020, the European Space Agency (ESA) raised the CS2 orbit into resonance with NASA's IS2, and a rephasing in July 2022 increased coincidence density over the Southern Ocean (Fredensborg Hansen et al., 2025a, 2025b), enabling systematic dual-altimetry coverage of the Antarctic sea-ice zone across the 2022–2025 annual cycles.

The only Antarctic calibration and validation studies of the C2I configuration to date have been conducted in the Weddell Sea, comprising airborne under-flight analyses by Fredensborg Hansen et al. (2025a); Fredensborg Hansen et al. (2025b) and waveform-decomposition retrievals by Zhou et al. (2026a, 2026b). Fredensborg Hansen et al. (2025a) operated coincident airborne C/S-band, Ku-band (ASIRAS), and Ka-band radar altimeters along a dedicated C2I orbit in December 2022 and evaluated multiple frequency pairings for snow-depth estimation. At 25 km averaging scales, the spaceborne C2I snow thickness agreed with the airborne LaKu estimate to within a 0.03 m bias and 0.08 m RMSD (Fredensborg Hansen et al., 2025b). However, the campaign was conducted during austral summer when wet-snow conditions limit Ku-band penetration (Willatt et al., 2023), and the spaceborne result was highly sensitive to the CS2 retracking methodology (Fredensborg Hansen et al., 2025b). In a complementary analysis, Zhou et al. (2026b) used a physics-based waveform model and convolutional neural network to decompose Ku-band CS2 waveforms over the Weddell Sea into snow-surface, snow-volume, and ice-surface contributions. They found that snow-volume scattering is comparable to or exceeds the ice-surface return under typical Antarctic conditions. Zhou et al. (2026a) derived snow depth from 46 C2I tracks in the Weddell Sea (2020–2022) using an optimized Threshold First-Maximum Retracker Algorithm (TFMRA)-70 retracker, confirming that the choice of retracking algorithm substantially affects the retrieved snow thickness. Together, these studies establish important observational benchmarks for the C2I configuration over Antarctic sea ice, but they are drawn exclusively from the Weddell Sea sector and from limited time windows that do not span the full post-2022 rephased configuration.

Although the LaKu concept is now established, its application over Antarctic sea ice remains constrained by three unresolved issues. First, most spaceborne Antarctic applications have relied on gridded freeboard differences or limited Weddell Sea case studies, so no study has yet exploited the post-2022 rephased C2I configuration to perform a systematic multi-winter along-track analysis across multiple sectors. Second, the Weddell and Ross seas, Antarctica's two largest sea-ice areas, differ markedly in sea-ice dynamics, precipitation patterns, and snow accumulation history (Arndt et al., 2024, 2025; Massom et al., 2001), yet the extent to which along-track dual-altimetry retrievals reproduce this expected regional contrast has not been quantified in a consistent multi-year framework. Third, the relationship between LaKu-derived snow thickness and the AMSR2 passive-microwave snow-depth product (Markus & Cavalieri, 1998; Meier et al., 2018) remains poorly understood at the retrieval scale, where spatial support, temporal compositing, and measurement physics differ substantially. Quantifying this relationship matters for two reasons. AMSR2 is the only long-term circumpolar Antarctic snow-depth record and therefore the de facto benchmark against which new retrievals are judged, so establishing where the two products agree and where they diverge is a prerequisite for interpreting either. More consequentially, snow depth is the dominant source of uncertainty in altimetry-derived sea-ice thickness, and the radiometer and dual-altimetry products are increasingly used as alternative snow inputs to that conversion; because the two rest on independent physics and error sources, the scale at which they agree determines whether they can be treated as interchangeable inputs, while their disagreement diagnoses the regimes in which each retrieval is least reliable. A systematic comparison across retrieval, gridded, and sector-mean scales is therefore needed to establish what the two products can and cannot jointly constrain.

Here, we use near-coincident IS2 and CS2 observations from the post-2022 C2I configuration to estimate winter snow thickness over the Weddell and Ross Sea sectors from August 2022 to September 2025. The purpose is not to provide formal validation against ground truth, which is unavailable at the required space-time scale, but to evaluate the internal consistency, regional structure, formal uncertainty, AMSR2 agreement, and penetration sensitivity of along-track Antarctic LaKu snow-thickness estimates. Although the multi-winter record could in principle support a dedicated analysis of seasonal and inter-annual snow-depth variability, the dominant per-matchup uncertainty and the unresolved, ice-regime-dependent scattering horizon (quantified below) mean that absolute inter-annual changes cannot yet be separated from retrieval uncertainty. We therefore focus on what the data set can robustly establish, namely the relative regional structure and the sensitivity of the absolute magnitude to the penetration assumption, and leave a dedicated variability analysis to future work once the scattering horizon is better constrained. Specifically, we ask: (a) whether the Weddell–Ross snow-thickness contrast is consistently resolved across months and years; (b) which formal error sources dominate the propagated per-matchup precision; (c) how C2I and AMSR2 snow-depth estimates differ across retrieval-scale, gridded, and sector-mean comparisons; and (d) how strongly the absolute retrieved snow thickness depends on the assumed Ku-band penetration factor, and which features of the retrieval are robust to that assumption. The fourth question is central: by quantifying the sensitivity of the absolute magnitude to the unresolved scattering horizon, and by identifying the penetration factor that reconciles the retrieval with an independent passive-microwave product, we aim to establish which features of along-track Antarctic dual-altimetry retrieval are robust and which remain conditional on retrieval assumptions. The remainder of the paper is organized as follows. Section 2 describes the satellite, ancillary, and reference data sets. Section 3 presents the collocation, retrieval, and uncertainty methodology. Section 4 reports the sector-scale snow-thickness retrievals, formal precision, AMSR2 comparison, and Ku-band penetration sensitivity. Section 5 interprets the results in the context of physical drivers and prior literature, and Section 6 concludes.

2. Data

This study combines three classes of satellite observations: IS2 laser freeboard from NASA, CS2 Ku-band radar freeboard from ESA, and AMSR2 passive-microwave snow depth. The IS2 and CS2 products provide the laser–radar freeboard pair from which snow thickness is retrieved at the along-track matchup scale, while the AMSR2 product serves as an independent benchmark for evaluating the retrieval at sector and gridded scales.

2.1. ICESat-2 Sea-Ice Products

NASA's IS2 is a photon-counting laser altimeter with six beams arranged as three pairs of strong (higher energy) and weak (lower energy) beams (Neumann et al., 2019). We use the ATL10 Sea-Ice Freeboard product (Version 7; Kwok et al. (2025)), which reports total freeboard relative to a local sea-surface reference determined from open-water leads identified within along-track segments of approximately 10 km length. Each ATL10 freeboard segment is derived from the underlying ATL07 sea-ice height segments (Kwok et al., 2025), with effective along-track resolutions of approximately 15 m for strong beams and 30 m for weak beams (Kwok et al., 2025). Per-beam freeboard, per-segment uncertainty, and quality flags are read from each granule; the effective along-track resolutions quoted above follow the ATL07/ATL10 product description of Kwok et al. (2025). These individual beam-level freeboard segments serve as input to the cross-sensor collocation: all beam segments within a 5 km search radius around each CS2 measurement are combined via inverse-distance weighting (IDW) to produce a single matched IS2 freeboard estimate. All six IS2 beams (three strong and three weak) are used throughout this study; we retain the weak beams, rather than restricting the analysis to the strong beams as some freeboard studies do, to maximize along-track sampling density at each CS2 location.

2.2. CryoSat-2 Radar Altimetry Products

ESA's CS2 carries the Synthetic Aperture Radar (SAR) Interferometric Radar Altimeter (SIRAL), which operates in SAR mode over Antarctic sea ice (Wingham et al., 2006). SAR-mode processing yields an along-track resolution of approximately 300 m per beam-formed sample at the 20-Hz posting rate, while the pulse-limited cross-track footprint is approximately 1.65 km in diameter. Our primary radar-freeboard source is the CS2 SAR-mode Level-2 Baseline-E product (European Space Agency, 2021a, 2021b), from which we extract the radar freeboard, surface-type flag, and the associated geolocation, the latter referenced to the point of closest approach (POCA), the location on the surface nearest to the satellite from which the dominant radar return originates. This product was selected as the primary Ku-band freeboard source for three reasons. First, our earlier intercomparison (Liu et al., 2025) evaluated four CS2 Baseline-E freeboard products over the Antarctic sea-ice zone: the Climate Change Initiative (CCI), the product from the Laboratoire d'Études en Géophysique et Océanographie Spatiales (LEGOS), the CryoSat-2 Antarctic Ocean (CSAO) product, and the CryoSat ThEMatic PrOducts (Cryo-TEMPO). Benchmarked against the CCI reference, ESA Baseline-E exhibited the most consistent performance across the Weddell and Ross Sea sectors and the smallest inter-product freeboard spread. Second, ESA Baseline-E is the same operational product adopted by Fredensborg Hansen et al. (2024) for the first Arctic C2I snow-depth analysis, facilitating cross-hemispheric comparison of the LaKu retrieval. Third, Baseline-E is ESA's most current operational sea-ice product and is widely used across the sea-ice altimetry community, which makes it the most appropriate baseline for a systematic Antarctic retrieval. We acknowledge that recent studies have shown a strong dependence of retrieved snow thickness on the choice of Ku-band retracking methodology (Fredensborg Hansen et al., 2025a, 2025b; Zhou et al., 2026a, 2026b), and we treat this retracker dependence as a limitation of the present analysis.

2.3. Auxiliary and Benchmark Data

We use the AMSR2 snow-depth product as an independent benchmark for the C2I retrievals. We obtain the snow-depth field from the AMSR-E/AMSR2 Unified Level-3 Daily 12.5 km Brightness Temperatures, Sea-Ice Concentration, Motion, and Snow Depth Polar Grids product (Version 1; Meier et al. (2018)), which applies the dual-frequency algorithm of Markus and Cavalieri (1998) to brightness temperatures composited over a five-day window. The product is distributed on a 12.5 km Southern Hemisphere polar stereographic grid, and we use the five-day running composite of snow depth. The retrieval assumes dry snow and is masked where conditions are wet (Markus et al., 2017); estimates over MYI are also masked where volume-scattering indicators apply.

The AMSR2 five-day compositing introduces a scale mismatch relative to the C2I along-track retrievals. Antarctic sea-ice drift during the five-day averaging window can reach 50 km or more in the Weddell and Ross gyres (Kwok & Maksym, 2014; Tian et al., 2023), so the AMSR2 brightness-temperature composite at each 12.5 km grid cell effectively integrates over a drift-smeared area of order 10^2–10^3 km^2. By contrast, each C2I along-track matchup samples an effective footprint of order 10 km^2, set by the CS2 SAR-mode pulse-limited footprint and the IS2 IDW-averaged segments within the 5 km collocation radius. The resulting one- to two-order-of-magnitude scale difference is an inherent limitation of any retrieval-scale comparison between these two products and contributes to the low point-to-point correlations.

3. Methods

The methodology comprises four steps: definition of the study domain and sector boundaries (Section 3.1); cross-sensor collocation of CS2 and IS2 observations with quality control (Section 3.2); retrieval of snow thickness from the freeboard difference (Section 3.3); and propagation of measurement uncertainties through the retrieval (Section 3.4). Two further subsections describe the AMSR2 benchmarking framework (Section 3.5) and the spatial-autocorrelation analysis used to compute effective sample sizes for significance testing (Section 3.6).

3.1. Study Domain and Sector Definitions

We analyze C2I observations over the Antarctic sea-ice zone from August 2022 to September 2025, spanning four austral winter-spring cycles following the July 2022 rephasing of the CS2 orbit that increased coincidence density over the Southern Ocean. The analysis focuses on two sectors: the Weddell Sea (62°W–15°E) and the Ross Sea (160°E–140°W). Within the Weddell Sea sector, we further distinguish a western sub-region (62°W–45°W), where recirculated MYI dominates, from an eastern sub-region (45°W–15°E), where seasonal first year ice (FYI) prevails (Arndt et al., 2024, 2025; Melsheimer et al., 2023). These sectors are selected for three reasons:

1. The Weddell and Ross seas encompass the two largest areas of Antarctic sea ice and together account for the majority of the circumpolar Antarctic sea-ice volume.
2. The sectors sample contrasting ice-age regimes (Arndt et al., 2021, 2024, 2025; Massom et al., 2001). The western Weddell Sea contains a substantial fraction of recirculated second-year and multi-year ice, whereas the eastern Weddell and Ross sectors are dominated by seasonal FYI. These differences provide contrasting snow accumulation histories, surface roughness, and potential radar-scattering regimes.
3. The Weddell and Ross seas have been the focus of the most extensive in situ and airborne sea-ice campaigns to date, including the Cryo2IceEx/NERC DEFIANT under-flight of a C2I orbit in the Weddell Sea (Fredensborg Hansen et al., 2025a, 2025b), providing broader observational context for interpreting satellite-derived retrievals.

Results are presented by sector and by month to resolve regime-dependent snow and radar-scattering behavior.

3.2. Cross-Sensor Collocation and Quality Control

For each CS2 20-Hz radar freeboard measurement (∼300 m along-track posting), we identify all IS2 ATL10 beam freeboard segments within a search radius $R = 5$ km and an orbit-level temporal separation $\delta t < 4$ h, following the C2I framework of Fredensborg Hansen et al. (2024). These collocation criteria are applied across the entire study period (August 2022–September 2025) for all observations south of 50°S. Each matchup aggregates hundreds to thousands of individual IS2 beam-level freeboard segments (∼15–30 m resolution) around a single CS2 measurement location, producing a spatially representative average at the ∼10 km collocation scale (the diameter of the search window). The search radius of $R = 5$ km is a modest enlargement of the $R = 3.5$ km radius used by Fredensborg Hansen et al. (2024) for their first Arctic C2I analysis and subsequently adopted by Fredensborg Hansen et al. (2025b) for their Weddell Sea airborne–satellite comparisons. The enlargement was adopted to accommodate the wider cross-track separation between CS2 and IS2 ground tracks at Antarctic latitudes during the post-2022 orbital configuration, which would otherwise exclude a substantial fraction of otherwise-valid matchups under the $n_j \geq 10$ retention criterion.

A sensitivity test across all 20 austral winter months analyzed here (2022–2025) confirms that the $R = 5$ km choice retains approximately 15% more matchups than $R = 3.5$ km (82,341 vs. 71,302) while the sector-median snow thickness shifts by less than 2 mm in both the Weddell and Ross sectors, well below the 38 mm per-matchup uncertainty (Section 4.4). Enlarging the radius further to $R = 7$ km yields approximately 14% additional matchups (94,183 in total) but at the cost of coarser effective spatial resolution and no material change in the sector-median snow thickness (shifts of less than 2 mm in both sectors), confirming that the 5 km choice is well-positioned in the yield–resolution trade-off.

Zhou et al. (2026a) applied a different along-track C2I collocation strategy over the Weddell Sea during 2020–2022, constraining matchups through a three-hour temporal coincidence window and averaging IS2 freeboard across all six beams from ATL07 at each CS2 location, and reported that their snow-depth estimates remained sensitive to the choice of CS2 retracking algorithm (TFMRA-70 vs. Baseline-E vs. TFMRA-50) rather than to the collocation geometry itself, a sensitivity that we recognize as a limitation of the present study.

The larger radius is compensated by the IDW averaging of all qualifying IS2 beam segments within R, which preserves spatial representativeness at the matchup scale (Equation 1):

$$h_{f,j}^{\mathrm{IS2}} = \frac{\sum_i w_i\, h_{f,i}^{\mathrm{IS2}}}{\sum_i w_i}, \qquad w_i = \frac{1}{d_i} \tag{1}$$

where d_i is the distance between the CS2 POCA location and the i-th IS2 beam freeboard segment, and the sum runs over all IS2 segments (from all six beams) within R. Matchups are retained only where at least 10 IS2 segments contribute ($n_j \geq 10$), ensuring that the IDW mean is computed from a spatially-representative sample.

Prior to collocation, quality-control filters are applied to both data products. On the IS2 side, ATL10 segments with a freeboard-quality flag larger than 1 are excluded; flag values of 0 and 1 indicate segments that passed the ATL10 quality checks, while values >1 flag segments with degraded freeboard estimates due to insufficient leads, poor sea-surface reference determination, or ambiguous surface-type classification (Kwok et al., 2025). Total freeboard values outside the range −0.5 to 5.0 m are excluded as physically unrealistic. On the CS2 side, measurements classified as non-sea-ice or with radar freeboard outside −1.0 to 10.0 m are removed. The wider retention window applied to the radar freeboard reflects its larger measurement noise and the possibility of negative radar freeboards where the scattering horizon lies within the snowpack, whereas the laser freeboard, referenced to the air–snow interface, is physically bounded more tightly; in practice both windows are permissive and reject only gross outliers. No explicit sea-ice drift correction is applied between paired CS2 and IS2 observations. The effective spatial scale of the collocated observations (~10 km diameter) is substantially broader than the typical sea-ice drift over the <4 h orbit-level coincidence interval: monthly drift speeds in the Weddell Sea are generally below 10 km d^{-1} (Kwok & Maksym, 2014; Tian et al., 2023), implying hourly displacements of order 0.5 km, which is well within the collocation window. Drift-induced mismatch is therefore expected to contribute collocation noise rather than systematic bias at the spatial scale adopted here.

3.3. Snow-Thickness Retrieval

We estimate snow thickness from the difference between the IDW-averaged IS2 total freeboard and the (speed of light in snow-corrected) CS2 radar freeboard at each matched observation. The retrieval is performed at each CS2 measurement location where a valid IDW-averaged IS2 freeboard and associated uncertainty are available.

The IS2 laser reflects from near the air–snow interface, while the CS2 Ku-band radar signal penetrates the snowpack toward the snow–ice interface but propagates through the snow layer at a reduced speed $c_s = c/\eta_s$, where c is the speed of light in vacuum and η_s is the refractive index of dry snow (Kacimi & Kwok, 2020; Kwok et al., 2020; Liu et al., 2025; Ulaby et al., 1986). Because the satellite altimeter computes range assuming speed c everywhere, the CS2-derived surface elevation is displaced below the true snow–ice interface by $h_s(\eta_s - 1)$, where h_s is the snow thickness. The IS2 laser freeboard reflects from near the air–snow interface and is given by Equation 2:

$$h_{f,j}^{\mathrm{IS2}} = h_i + h_s, \tag{2}$$

While the CS2 radar freeboard is referenced to the snow-delayed ice interface and is given by Equation 3:

$$h_{f,j}^{\mathrm{CS2}} = h_i - h_s(\eta_s - 1), \tag{3}$$

where h_i is the sea-ice freeboard at matchup j. The freeboard difference is therefore $\Delta f_j = h_{f,j}^{\mathrm{IS2}} - h_{f,j}^{\mathrm{CS2}} = h_s \cdot \eta_s$ under the assumption of complete Ku-band penetration to the snow–ice interface. We emphasize that two physically distinct effects act on the Ku-band measurement and are treated separately here. The first is the propagation delay represented by η_s in Equations 3 and 5, which arises because the radar travels more slowly through snow than through vacuum and displaces the apparent surface downward by a fixed amount for a given

10.1029/2026EA005247

snow column. The second is the position of the dominant scattering horizon within the snowpack, which need not coincide with the snow–ice interface and which we represent by a penetration factor $\delta \in (0, 1]$ that scales the effective freeboard difference attributable to the snow layer. The propagation delay is a deterministic correction; the scattering-horizon position is the principal physical unknown. With both effects included, the snow thickness at matchup j is given by Equation 4:

$$h_{s,j} = \frac{\Delta f_j}{\delta \cdot \eta_s} \tag{4}$$

The refractive-index correction η_s is parameterized (Equation 5) following the Ku-band dry-snow formulation of Ulaby et al. (1986) as implemented in the IS2–CS2 freeboard-difference framework of Kwok et al. (2020), Kacimi and Kwok (2020), Fredensborg Hansen et al. (2024), and Fredensborg Hansen et al. (2025b):

$$\eta_s = \left(1 + 0.51\,\rho_s\right)^{1.5} \tag{5}$$

where ρ_s is the snow density in g cm^{-3}. For a baseline density of $\rho_s = 0.33$ g cm^{-3} (330 kg m^{-3}), this yields $\eta_s = 1.263$, giving a propagation correction of $1/\eta_s = 0.792$. The dry-snow permittivity of Ulaby et al. (1986) is frequency independent across the microwave range for dry-snow conditions (Tiuri et al., 1984) and is therefore applicable at the CS2 Ku-band frequency of 13.575 GHz. Substituting the Tiuri et al. (1984) dry-snow permittivity ($\varepsilon' = 1 + 1.7\,\rho_s + 0.7\,\rho_s^2$, yielding $n_s = 1.279$) changes the retrieved snow thickness by less than 2%, which we treat as negligible relative to the per-matchup uncertainty quantified in Section 3.4. The retrieval is restricted to the austral winter months (May–October) when dry-snow conditions best satisfy this assumption. Because the CS2 orbit rephasing was completed in July 2022, the first winter (2022) contains only August–October data; the 2023 and 2024 winters each span the full May–October period; and the 2025 winter covers May–September. Snow-density uncertainty is set to $\sigma_\rho = \pm 0.07$ g cm^{-3} following Kacimi and Kwok (2020); its propagation into h_s is described later.

We adopt a baseline penetration factor $\delta = 0.70$ (denoted α in the convention of Nab et al. (2024)) as a reference scenario for the primary numerical summary, not as a validated Antarctic penetration depth, which reflects the literature consensus of 60%–90% Ku-band penetration into snow on Arctic sea ice (Landy et al., 2026; Nab et al., 2024) and is consistent with recent empirical evidence that Ku-band radar freeboards track the snow–ice interface during cold winter conditions over Arctic FYI (Taelman et al., 2026). Over Antarctic sea ice, the effective penetration depth is less well constrained because saline snow, internal ice lenses formed through melt–refreeze cycles, and other snowpack heterogeneities may further limit Ku-band penetration ($\delta < 1$), particularly over FYI with brine-wetted basal layers (Arndt et al., 2024, 2025; Fredensborg Hansen et al., 2025a; Geldsetzer et al., 2009; Mallett et al., 2024; Nandan et al., 2017; Willatt et al., 2023; Zhou et al., 2026a). Occasional negative $h_{s,j}$ values are retained rather than set to zero, because random measurement errors over thin-snow regimes can produce small negatives that, if truncated, would introduce a positive bias into the distribution. The sensitivity of the retrieved snow thickness to the choice of δ, including the full-penetration upper bound ($\delta = 1$), is quantified in the Results and interpreted in the Discussion.

3.4. Formal Per-Matchup Precision

We estimate the formal per-matchup precision of the retrieved snow thickness by propagating measurement-level IS2 and CS2 freeboard uncertainties and snow-density uncertainty through $h_s = \Delta f / \eta_s$ in quadrature, conditional on the selected penetration factor δ. This formal precision should not be interpreted as the total retrieval uncertainty, because it excludes structural errors associated with the unknown Ku-band scattering horizon, retracker dependence, residual collocation mismatch, and unresolved sub-footprint snow heterogeneity.

3.4.1. Freeboard Uncertainties

The IS2 total freeboard uncertainty $\sigma_{\mathrm{IS2},j}$ is taken as the mean of the ATL10 product-reported per-segment uncertainties for all IS2 beam freeboard segments contributing to the IDW mean at matchup j. This term incorporates photon-counting statistics, surface-finding algorithm precision, and reference sea-surface height uncertainty as propagated within the ATL10 processing chain (Kwok et al., 2025). We note that the segment-level uncertainties are arithmetically averaged rather than IDW-weighted; in practice, the ATL10 per-segment uncertainties are sufficiently uniform within each matchup that the difference is negligible relative to other error sources. The CS2 radar freeboard uncertainty σ_{CS2} is set to a constant value of 0.03 m per 20-Hz measurement, representing a conservative estimate of the combined instrument noise and retracking uncertainty for a single CS2 SAR-mode measurement over sea ice (Wingham et al., 2006). Unlike the IS2 term, this CS2 uncertainty is held constant because the Baseline-E product does not provide a matchup-specific retracking uncertainty over sea ice; it therefore enters Equation 6 as a fixed value at every matchup. We therefore prescribe $\sigma_{CS2} = 0.03$ m as a representative measurement-scale scenario rather than a product-derived uncertainty. A direct consequence is that the matchup-to-matchup variability in the total per-matchup precision is governed almost entirely by the spatially varying IS2 term, while the CS2 term contributes a near-constant floor, as quantified in Section 3.4. The penetration factor δ is not included in the formal uncertainty budget because it cannot be independently constrained from spaceborne data alone; its effect is instead characterized through the sensitivity analysis. That analysis (Section 4.6) shows that the absolute retrieved snow thickness scales inversely with δ, so that halving δ from 1.00 to 0.50 approximately doubles the inferred thickness in both sectors, whereas the Weddell–Ross contrast, the negative-retrieval fraction, and the AMSR2 correlation are all invariant to the choice of δ. The value $\delta^* \approx 0.55$ brings the sector-median estimates into closest agreement with AMSR2.

$$\sigma^2_{h_s,j} = \frac{\sigma^2_{IS2,j} + \sigma^2_{CS2}}{(\delta \cdot \eta_s)^2} + \left(\frac{\Delta f_j \cdot \sigma_{\eta_s}}{\delta \cdot \eta_s^2}\right)^2 \tag{6}$$

3.4.2. Snow-Density (Refractive-Index) Uncertainty

The sensitivity of η_s to snow density is obtained by differentiating Equation 5 (Equation 7):

$$\frac{d\eta_s}{d\rho_s} = 1.5 \times 0.51 \times (1 + 0.51\,\rho_s)^{0.5} \tag{7}$$

For $\rho_s = 0.33$ g cm^{-3}, this gives $d\eta_s/d\rho_s = 0.859$. With $\sigma_\rho = 0.07$ g cm^{-3}, the propagated uncertainty on η_s is $\sigma_{\eta_s} = 0.060$. We also conduct several snow-density sensitivity tests and present them in Appendix A. Sensitivity tests confirm that these retrievals are robust to the principal snow-related assumptions (Appendix A). Varying the assumed snow density across the plausible Antarctic range ($\rho_s = 260$–400 kg m^{-3}) shifts the retrieved mean snow thickness by only 0.023 m in the Weddell Sea and 0.020 m in the Ross Sea, both smaller than the 0.040 m mean per-matchup precision. Critically, the Weddell–Ross sector contrast is preserved at every density tested (0.037–0.040 m). Substituting the Tiuri et al. (1984) dry-snow permittivity for the baseline Ulaby et al. (1986) parameterization alters the retrieved thickness by less than 2%. The absolute magnitude is therefore controlled not by the snow-density or permittivity assumptions but by the unresolved radar penetration depth (Section 4.6).

3.4.3. Total Per-Matchup Uncertainty

Since $h_{s,j} = \Delta f_j/(\delta \cdot \eta_s)$, the per-matchup snow-thickness uncertainty follows from standard error propagation. The freeboard uncertainties are scaled by $1/(\delta \cdot \eta_s)$, which is the same factor that converts the freeboard difference to snow thickness, and the density uncertainty enters through the sensitivity of η_s to ρ_s. Under the assumption of mutual independence among the three error components, the total per-matchup snow-thickness variance is given by Equation 6.

For the baseline density of 330 kg m^{-3} (yielding $\eta_s = 1.263$) and $\delta = 0.70$, the scaling factor $1/(\delta \cdot \eta_s) = 1.130$, so the CS2 contribution to the snow-thickness uncertainty is $\sigma_{CS2}/(\delta \cdot \eta_s) = 0.030/0.884 = 0.034$ m per matchup, and the IS2 contribution is typically ~0.005–0.010 m, varying with photon-counting conditions at each matchup. The density term is proportional to the freeboard difference Δf_j and therefore increases with snow thickness; at the mean snow thickness ($h_s \approx 0.26$ m) it contributes ~0.006 m. The CS2 freeboard uncertainty therefore dominates the total budget, providing a near-constant floor of ~0.034 m per matchup. This instrument-dominated precision is sector-independent and should be distinguished from the systematic, sector-dependent bias introduced by the unknown Ku-band scattering horizon, which is not part of the formal precision and is discussed separately in Sections 5.2 and 5.7.

Table 1
Along-Track Spatial Autocorrelation and Effective Sample Size for the Austral Winter (May–October) CRYO2ICE Matchups

Sector	n	r_1	Decorr. (km)	n_{eff}	n_{eff}/n (%)
Weddell Sea	47,735	0.39	9	20,948	44
Ross Sea	34,606	0.39	10	15,187	44

Note. The lag-1 autocorrelation r_1 is the classical index-shift value computed at the CryoSat-2 posting interval (~0.31 km). The decorrelation length is the first zero crossing of the native-resolution autocorrelation function. n_{eff} is computed in Section 3.6.

Three assumptions and limitations of this formal uncertainty model are noted. First, the quadrature combination assumes independence among error sources; while IS2 and CS2 instrument errors are independent by construction, shared surface conditions may introduce correlated geophysical variability, so the resulting formal uncertainty is conservative. Second, the baseline penetration factor $\delta = 0.70$ is treated as fixed in the uncertainty budget. although the true scattering horizon is uncertain and may vary with ice type, snow stratigraphy, and brine content (Fredensborg Hansen et al., 2025a, 2025b; Zhou et al., 2026a, 2026b); the sensitivity of h_s to δ is treated separately rather than as a contribution to the formal precision. Third, the IS2 freeboard standard deviation within each matchup, which captures sub-footprint surface heterogeneity within the 5 km collocation radius, is reported as a diagnostic but is not included in the formal uncertainty estimate. The sensitivity of the retrieval to the assumed snow density is evaluated separately by recomputing h_s at $\rho_s = 260, 330$, and 400 kg m^{-3}, with results reported in Appendix A.

3.5. Benchmarking Against AMSR2 Snow Depth

To evaluate the along-track C2I snow-thickness retrievals against an independent basin-scale reference, we compare them with the AMSR2 gridded snow-depth product (Section 2.3). For each C2I matchup, the nearest AMSR2 grid cell for the corresponding date is extracted using a nearest-neighbor query. Matchups are excluded where the AMSR2 product reports invalid snow depth, for example, under wet-snow or strong volume-scattering conditions. We report the mean and median difference (C2I − AMSR2), the RMSD, and the Pearson correlation coefficient for each sector and month, with both mean and median statistics reported to accommodate the right-skewed nature of Antarctic snow-thickness distributions. Because neither product can be assumed to represent ground truth, the comparison is framed as mutual benchmarking rather than formal validation, and systematic differences between the two products are interpreted in the Discussion in the context of measurement physics, spatial scales, and known retrieval limitations.

3.6. Effective Sample Size and Spatial Autocorrelation

Adjacent along-track matchups share overlapping IS2 footprints within the 5 km collocation radius and are therefore spatially autocorrelated. To account for this non-independence, we estimate the effective number of independent observations as $n_{\mathrm{eff}} = n(1 - r_1)/(1 + r_1)$, following Mitchell et al. (1966), where r_1 is the lag-1 along-track autocorrelation.

The autocorrelation function is computed within each orbit track at the native CS2 posting interval (~0.31 km) using the classical index-shift method. Orbit tracks are identified by grouping consecutive matchups from the same date with along-track gaps below 50 km, and the autocorrelation is pooled across all tracks with at least 30 matchups using track-length weighting (286 Weddell Sea tracks, 225 Ross Sea tracks). At the CS2 measurement scale, the pooled lag-1 autocorrelation is $r_1 = 0.39$ in both sectors, with decorrelation lengths (defined as the first zero crossing of the native-resolution autocorrelation function) of 9 km in the Weddell Sea and 10 km in the Ross Sea (Table 1). The resulting effective sample sizes are $n_{\mathrm{eff}} = 20,948$ for the Weddell Sea (44% of $n = 47,735$) and $n_{\mathrm{eff}} = 15,187$ for the Ross Sea (44% of $n = 34,606$); these values are used in all significance tests and standard-error calculations reported below.

4. Results

We present the results in six subsections. Section 4.1 reports the collocation yield and sampling characteristics, Section 4.2 establishes the Weddell–Ross sector contrast in retrieved snow thickness, and Section 4.3 examines the seasonal evolution of snow thickness within each sector. Section 4.4 quantifies the formal per-matchup precision of the retrieval, Section 4.5 benchmarks the retrievals against the AMSR2 passive-microwave snow-depth product, and Section 4.6 characterizes the sensitivity of the retrieval to the assumed Ku-band penetration factor.

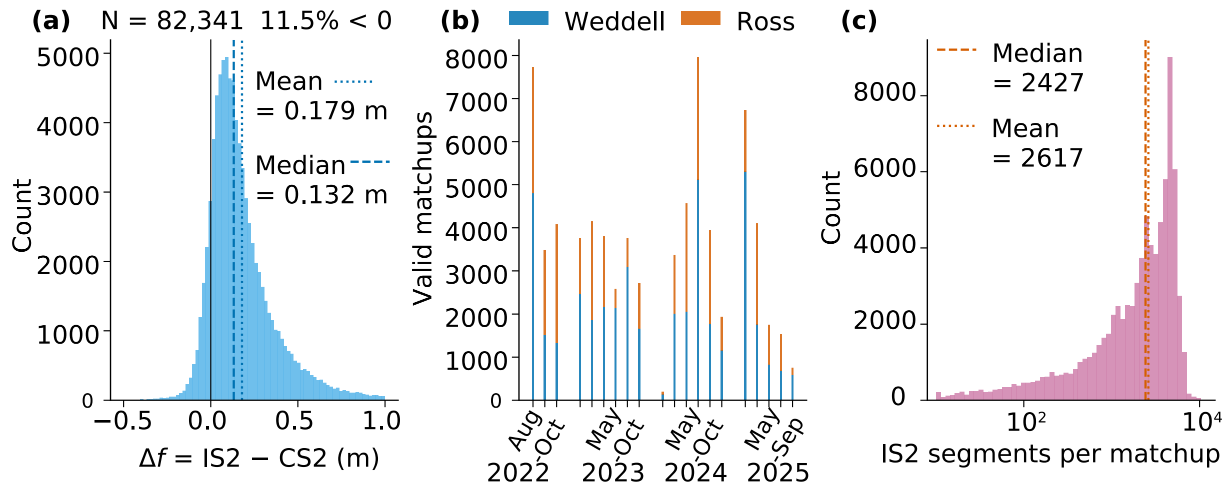

Figure 1. Collocation characteristics for the austral winter (May–October) CRYO2ICE data set, 2022–2025. (a) Distribution of the freeboard difference $\Delta f = h_f^{\mathrm{IS2}} - h_f^{\mathrm{CS2}}$ across all 82,341 Weddell and Ross winter matchups; the dashed line marks the median, the dotted line marks the mean, and 11.5% of matchups yield $\Delta f < 0$. The sector-specific analysis in subsequent sections is restricted to the Weddell Sea (47,735) and Ross Sea (34,606) subsets. (b) Monthly valid matchup counts for the Weddell Sea (blue) and Ross Sea (orange) sectors. (c) Number of ICESat-2 (IS2) beam freeboard segments contributing to each matchup (log scale).

4.1. Collocation Yield and Sampling Characteristics

The collocation framework yielded 82,341 winter (May–October) matchups across the four austral winters (2022–2025), comprising 47,735 in the Weddell Sea and 34,606 in the Ross Sea (Table C1). Of these, 88.9% in the Weddell Sea and 88.0% in the Ross Sea yield positive snow thickness estimates ($h_s > 0$), corresponding to 42,447 and 30,460 valid retrievals respectively. The nearly identical valid fractions across the two sectors indicate that the retrieval performs comparably under contrasting ice regimes, and the 11%–12% negative-retrieval fraction is consistent with random measurement errors in thin-snow conditions where Δf fluctuates around zero. Of these negative retrievals, approximately 5.1% are more negative than −0.05 m and only 2.2% are more negative than −0.10 m, confirming that the majority are small in magnitude and consistent with measurement noise rather than systematic error.

Three diagnostics characterize the sampling quality of the matchup data set. The distribution of the freeboard difference $\Delta f = h_f^{\mathrm{IS2}} - h_f^{\mathrm{CS2}}$ across the 82,341 winter matchups is right-skewed, with a mean of 0.179 m, a median of 0.132 m, and 11.5% of values falling below zero (Figure 1a). Monthly sampling density varies across the study period (Figure 1b), generally increasing from May toward August–September as sea-ice extent expands, although year-to-year differences in orbital geometry and ice conditions produce substantial variability between winter seasons. Each matchup aggregates a median of 2,427 and a mean of 2,617 IS2 beam freeboard segments (Figure 1c), confirming spatially dense IS2 sampling at each CS2 measurement location.

4.2. Snow Thickness: Weddell Sea Versus Ross Sea

Austral winter snow thickness in the Weddell Sea (mean 0.255 m, median 0.188 m) systematically exceeds that in the Ross Sea (mean 0.217 m, median 0.156 m) by 18% and 21%, respectively (Table C1). This contrast persists across all winter months and all 4 years of our study (Figures 2 and 3).

The probability density functions of retrieved snow thickness in each sector confirm the contrast (Figure 3a). Both distributions are right-skewed with long tails extending beyond 0.4 m. The Weddell Sea sector distribution has a higher median and a heavier upper tail than the Ross Sea sector distribution, reflecting the thicker snow that accumulates over MYI in the western Weddell Sea. The Ross Sea distribution is more concentrated near zero, consistent with thinner snow on younger, polynya-exported FYI. The cumulative distribution functions (CDFs) quantify this separation: the Weddell Sea CDF lies to the right of the Ross Sea CDF at every quantile (Figure 3c), indicating that the sector contrast is not driven by outliers but holds across the entire distribution. The interquartile ranges (IQRs; Weddell Sea: 0.097–0.339 m; Ross Sea: 0.081–0.277 m) overlap partially but the Weddell IQR is shifted consistently higher (Table C1), indicating substantial sub-sector heterogeneity in both regions together

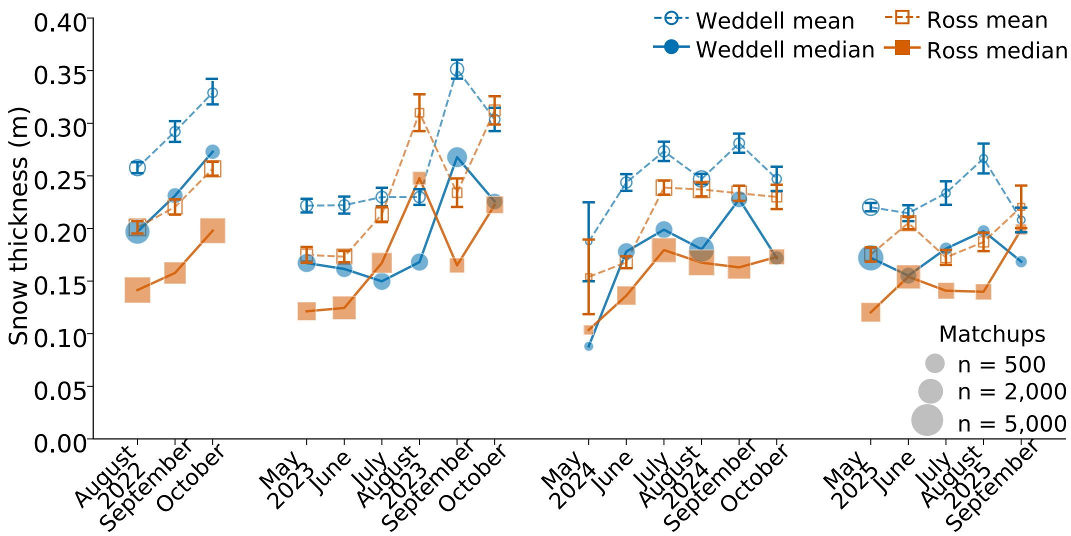

Figure 2. Temporal evolution of CRYO2ICE snow-thickness retrievals for the austral winter (May–October), 2022–2025. Monthly mean (dashed lines, open markers) and median (solid lines, filled markers) snow thickness are shown for the Weddell Sea (blue circles) and Ross Sea (orange squares). Marker size is proportional to the number of valid matchups per sector-month (smallest markers: $n \approx 500$; largest: $n > 5{,}000$). Lines connect months within each winter season but are not drawn across inter-annual gaps. Error bars on the mean markers denote ±1 autocorrelation-adjusted standard error of the monthly sector mean, computed as $\sigma_{h_s}/\sqrt{n_{\mathrm{eff}}}$ using the sector effective sample sizes of Section 3.6; medians are shown with semi-transparent markers so that overlapping error bars remain visible.

with a systematic upward shift of the full distribution in the Weddell Sea. The ice-type and accumulation differences that drive this contrast are examined in the Discussion.

The spatial distribution of snow thickness further resolves the sector contrast (Figure 4). Within the Weddell Sea sector, the thickest snow is concentrated in the western sub-region adjacent to the Antarctic Peninsula, where the prevalence of relatively thick MYI (Massom et al., 2001; Melsheimer et al., 2023) provides both a longer accumulation history and a rougher surface that retains deeper snow. Snow thickness decreases progressively

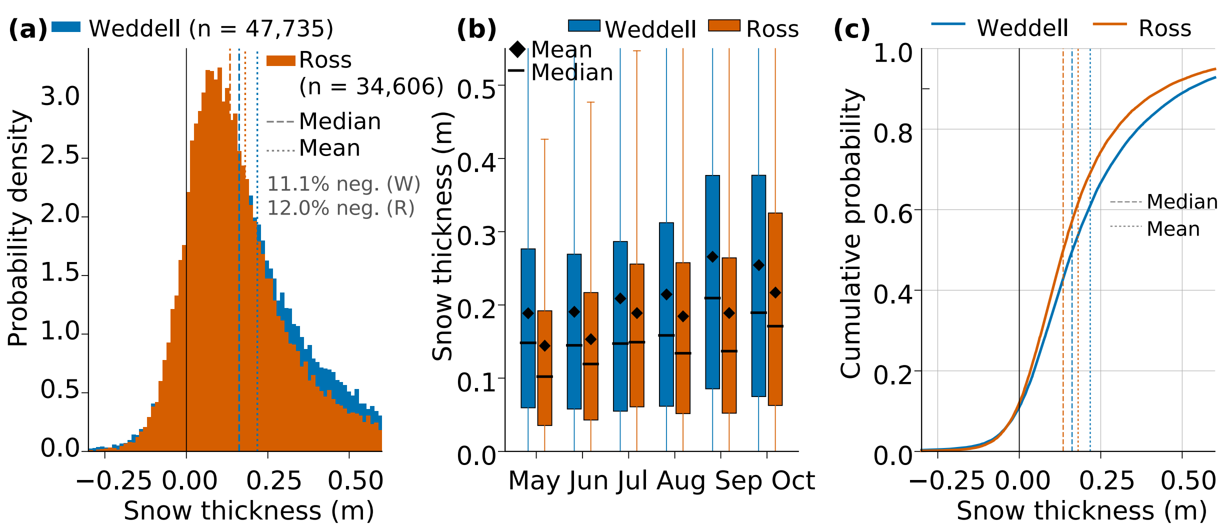

Figure 3. Regional snow-thickness distributions for the austral winter (May–October, 2022–2025), comparing the Weddell Sea and Ross Sea sectors. All retrievals are included, including the 11%–12% of matchups that yield negative snow thickness. (a) Probability density of retrieved snow thickness; dotted lines indicate sector means and dashed lines indicate sector medians. The vertical black line marks $h_s = 0$. (b) Monthly box plots showing the seasonal progression of snow thickness in each sector; boxes span the interquartile range (IQR), whiskers extend to 1.5 × IQR, black diamonds mark the mean and horizontal lines mark the median. (c) Cumulative distribution functions (CDFs); the Weddell CDF is shifted to the right of Ross at every quantile. Dotted and dashed vertical lines mark mean and median, respectively. The CDF includes negative retrievals, visible as the non-zero cumulative probability at $h_s = 0$ (approximately 11%–12% in both sectors).

10.1029/2026EA005247

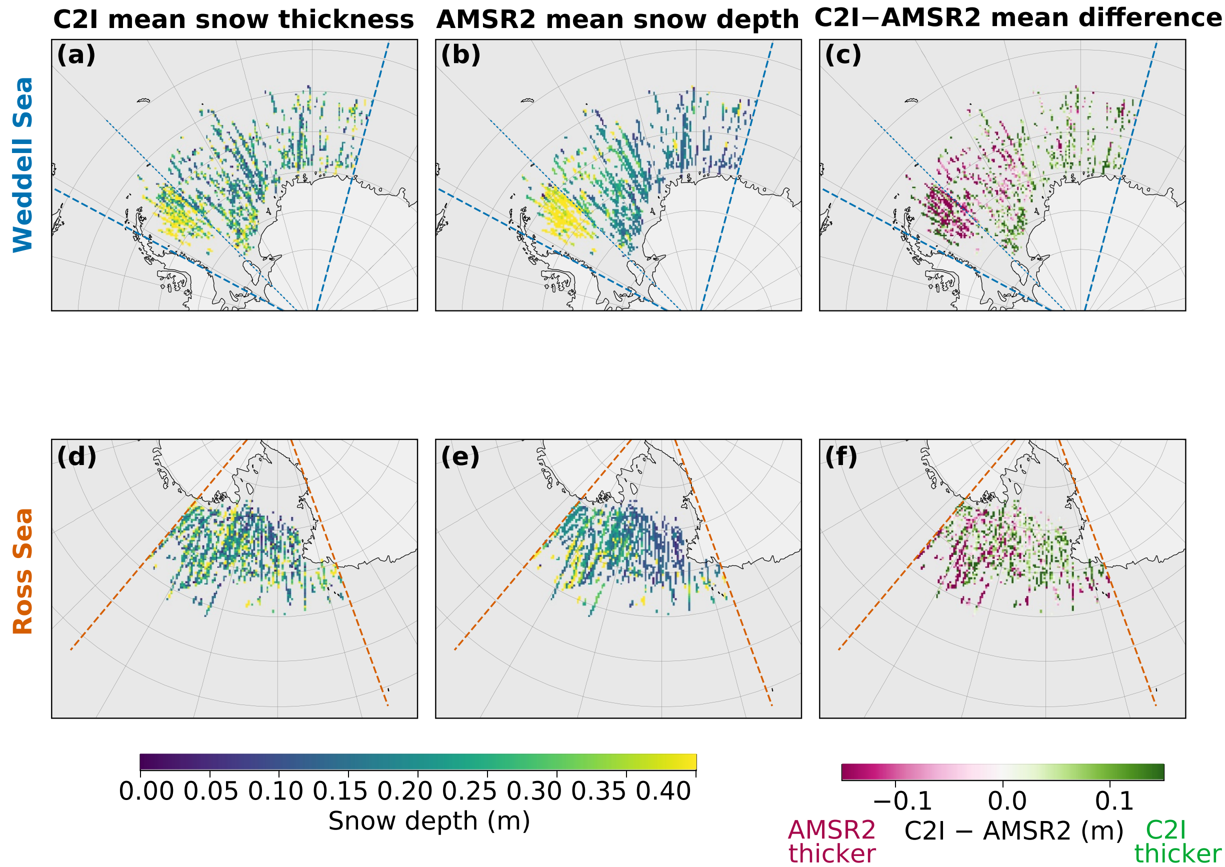

Figure 4. Gridded comparison of CRYO2ICE (C2I) snow thickness, Advanced Microwave Scanning Radiometer 2 (AMSR2) snow depth, and their difference on a 25 km National Snow and Ice Data Center (NSIDC) polar stereographic grid. Top row (a, b, c) Weddell Sea (62°W–15°E); bottom row (d, e, f): Ross Sea (160°E–140°W). Left column (a, d) mean C2I snow thickness per grid cell; middle column (b, e) mean AMSR2 snow depth per grid cell; right column (c, f) mean per-cell difference (C2I minus AMSR2), where green indicates C2I thicker and pink indicates AMSR2 thicker. Dashed lines mark the sector boundaries; in the Weddell panels, the dotted line at 45°W separates the western (MYI dominated) and eastern (FYI dominated) sub-regions. Gray areas indicate no data.

toward the eastern boundary of the sector near 15°E. The Ross Sea sector, by contrast, is characterized by thinner and more spatially uniform snow cover, with the lowest values near the Ross Sea Polynya and modestly thicker snow toward the outer pack ice. This spatial structure, with deep snow concentrated over the older ice of the western Weddell Sea and thin uniform snow over the polynya-fed Ross Sea pack, is the signature we attribute in Section 5.1 to the contrasting ice-age and deformation regimes of the two sectors.

4.3. Seasonal Evolution

Both sector means generally exhibit increasing snow thickness from May to October within each winter season, consistent with progressive accumulation on the sea-ice pack (Table C1; Figure 3b). This seasonal interpretation is limited to the observed months and is not treated as a continuous accumulation budget. In the Weddell Sea, monthly mean (median) snow thickness increases from 0.220 (0.169) m in May to 0.309 (0.236) m in September before decreasing slightly to 0.296 (0.219) m in October, a 34.5% (29.6%) increase in mean (median) over the winter period. Within the Weddell Sea, the western sub-region (west of 45°W) shows a muted seasonal progression consistent with a deeper, more metamorphosed initial snowpack on MYI, whereas the eastern sub-region (east of 45°W) shows stronger month-on-month accumulation consistent with a younger FYI snowpack responding to fresh precipitation events (Section 4.2). The Ross Sea shows a steadier progression, from 0.175 (0.120) m in May to 0.265 (0.198) m in October, a 51.4% (65.0%) increase in mean (median). The Weddell Sea mean and median snow thickness both exceed the corresponding Ross Sea values in every month, and the IQR widens from May to October in both sectors, indicating increasing surface heterogeneity as winter progresses and the snowpack develops.

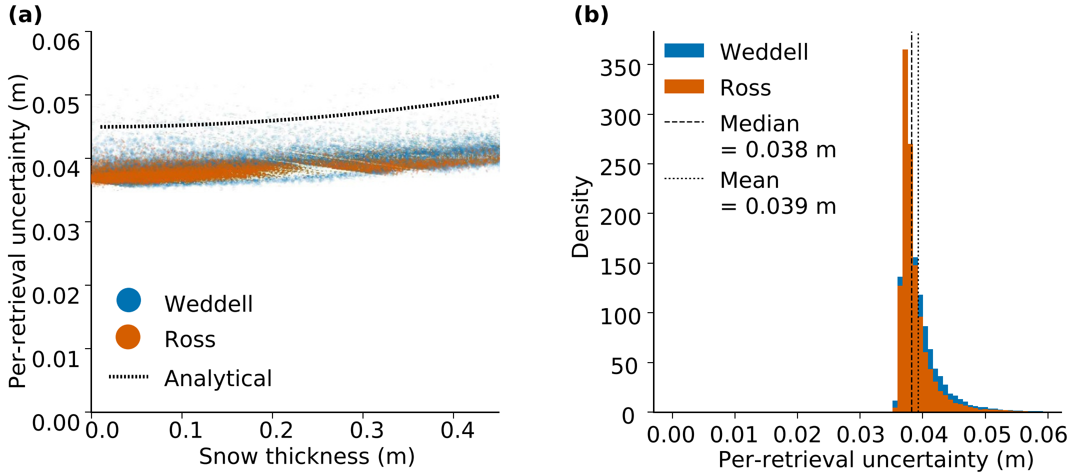

Figure 5. Per-matchup uncertainty of the snow-thickness estimates for the austral winter (May–October, 2022–2025). (a) Snow thickness versus per-matchup uncertainty for the Weddell Sea (blue) and Ross Sea (orange). The gray shaded band shows the analytical uncertainty model (Equation 6) evaluated across the 25th-to-50th percentile range of the ICESat-2 freeboard uncertainty observed in the data set. (b) Probability density of the per-matchup uncertainty, stratified by sector; the dotted line marks the mean and the dashed line marks the overall median.

The multi-year time series of monthly mean snow thickness (Figure 2) confirms that the Weddell–Ross contrast is robust across all four austral winters. The autocorrelation-adjusted standard error of each monthly mean (error bars in Figure 2) remains below 0.007 m in all sector-months and near 0.003 m in the best-sampled months, so that the Weddell–Ross separation and the seasonal increase are both large relative to the monthly sampling uncertainty. The Weddell Sea shows larger inter-annual variability than the Ross Sea sector, with the 2022 winter producing the highest Weddell medians (reaching 0.264 m in October 2022) and the 2024 winter showing more moderate values. The Ross Sea medians are more temporally stable, fluctuating within a narrower range (0.08–0.25 m) across all years. The contrast between the muted Weddell inter-annual signal and the steadier Ross progression is interpreted in terms of ice-type and snow-regime differences in the Discussion.

4.4. Per-Matchup Precision and Sensitivity to Snow Density

The mean per-matchup uncertainty represents 15.7% of the Weddell Sea mean snow thickness and 18.0% of the Ross Sea mean, and 20.2% and 24.4% of the respective sector medians (Table C1; Figure 5b). The near-identical uncertainty in both sectors demonstrates that the error budget is dominated by instrument measurement uncertainty rather than sector-dependent geophysical variability. This formal precision underestimates the total retrieval uncertainty because it excludes the residual uncertainty in the $\delta = 0.70$ penetration assumption, which may introduce a sector-dependent systematic bias if Ku-band penetration differs between the predominantly FYI of the Ross Sea and the MYI-bearing western Weddell Sea. The penetration contrast between these ice types arises from several mechanisms acting together, including basal brine over FYI but also snow metamorphism, grain growth, and superimposed ice over MYI (Section 5.2), rather than from salinity alone. This structural uncertainty is interpreted in the Discussion.

The three-component uncertainty model (Equation 6) reveals that the CS2 radar freeboard uncertainty is the dominant contributor, providing a near-constant floor of 0.034 m per matchup as established in Section 3.4. The IS2 freeboard uncertainty is the second-largest component, contributing a variable amount that depends on the photon-counting statistics and sea-surface reference quality at each matchup. The snow-density term is the smallest component for thin snow but increases with snow thickness because it is proportional to Δf. For the thickest Weddell Sea retrievals ($h_s > 0.3$ m), the density term contributes approximately 0.005 m additional uncertainty. The upward slope of the scatter cloud in Figure 5a is consistent with this density-dependent behavior; the analytical uncertainty curve (Equation 6, evaluated at the median IS2 uncertainty) lies above the scatter cloud because individual matchups have variable IS2 contributions that are generally smaller than the median.

Table 2
Advanced Microwave Scanning Radiometer 2 (AMSR2) Benchmarking Statistics for Austral Winter (May–October), Stratified by Sector

	Weddell sea	Ross sea
n	40,431	28,510
C2I mean (median) h_s (m)	0.256 (0.188)	0.216 (0.155)
AMSR2 mean (median) (m)	0.252 (0.200)	0.195 (0.170)
Mean (median) bias (m)	+0.004 (−0.012)	+0.021 (−0.015)
RMSD (m)	0.239	0.228
r	0.250	0.027
r^2	0.062	0.001
p-value (nominal n)	<0.001	<0.001
p-value (n_{eff})	<0.001	0.002

Note. Correlations and p-values are reported both at the nominal sample size n and at the effective sample size n_{eff} (Table 1). CRYO2ICE: C2I.

Sensitivity tests (Table A1, Appendix A) show that varying the assumed snow density across the plausible Antarctic range ($\rho_s = 260, 330$, and 400 kg m^{-3}) changes the retrieved mean snow thickness by less than the mean per-matchup uncertainty in both sectors. The Weddell–Ross contrast is preserved at every density tested (0.037–0.040 m mean difference), confirming that the sector contrast is insensitive to the density assumption. Substituting the permittivity formulation by Tiuri et al. (1984) for the parameterization by Ulaby et al. (1986) changes the retrieved snow thickness by less than 2%, which is negligible relative to the measurement uncertainty. That the dominant error source is the CS2 radar freeboard rather than any snow property is the basis for our argument in Section 5.4 that future precision gains will come from improved retracking rather than from refined snow climatologies.

4.5. Benchmarking Against AMSR2 Snow Depth

Over the AMSR2-matched subset of 40,431 Weddell Sea and 28,510 Ross Sea winter matchups, the C2I–AMSR2 difference depends on the descriptor (Table 2; Figure 6). Mean differences are small and positive in both sectors (Weddell Sea: +0.004 m; Ross Sea: +0.021 m), whereas median differences are negative (Weddell Sea: −0.012 m; Ross Sea: −0.015 m), indicating that the typical matchup has thinner C2I snow than AMSR2 but that the C2I distribution contains a sufficiently heavy upper tail to offset this in the mean. We therefore report both mean and median differences throughout, treating the median as the more robust descriptor of the retrieval-scale offset between two right-skewed distributions (Figure 7). The retrieval-scale root-mean-square difference (RMSD) between the two products is 0.239 m in the Weddell Sea and 0.228 m in the Ross Sea. Although the baseline retrieval adopts $\delta = 0.70$, which represents a literature-justified estimate of the Ku-band penetration depth rather than the full-penetration assumption, the sign of the C2I–AMSR2 bias is physically informative: AMSR2 snow depth exceeds C2I snow thickness even though incomplete Ku-band penetration ($\delta < 1$) is expected to cause C2I to underestimate true snow thickness.

The matchup density plots in Figure 6 show that the majority of matchups cluster below the 1:1 line in both sectors, confirming the systematic negative bias. The Weddell Sea comparison (Figure 6a) exhibits greater scatter and a wider range of AMSR2 values, reflecting the more heterogeneous snow conditions over MYI. In contrast, the Ross Sea comparison (Figure 6b) shows a tighter cluster concentrated at lower snow depths, consistent with the thinner, more uniform snow in this sector.

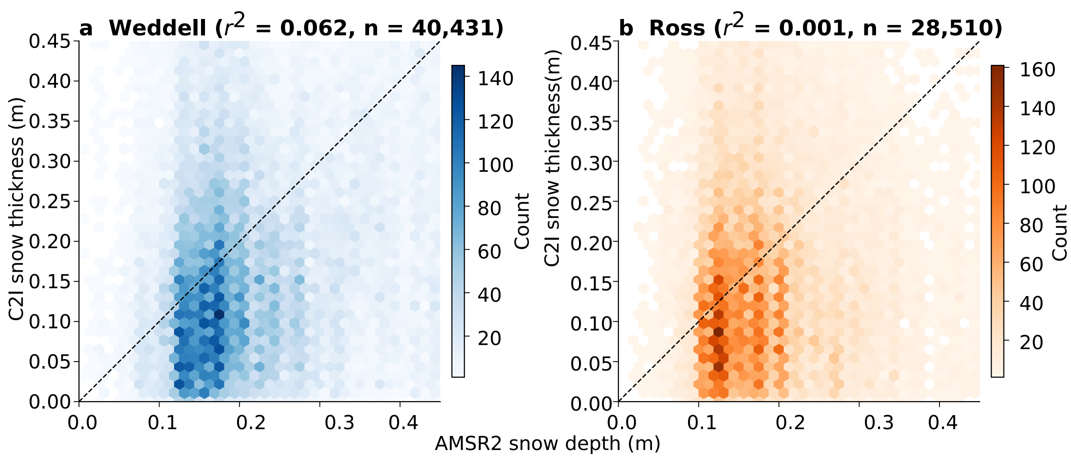

Figure 6. Benchmarking of CRYO2ICE (C2I) snow-thickness retrievals against Advanced Microwave Scanning Radiometer 2 (AMSR2) gridded snow depth for the austral winter (May–October, 2022–2025). (a) Weddell Sea and (b) Ross Sea matchup density hexagonal-bin density plots; the dashed black line in each panel indicates 1:1 agreement. Sample sizes are $n = 40,431$ for the Weddell Sea and $n = 28,510$ for the Ross Sea, reflecting the AMSR2-matched subset where AMSR2 reports valid snow depth.

10.1029/2026EA005247

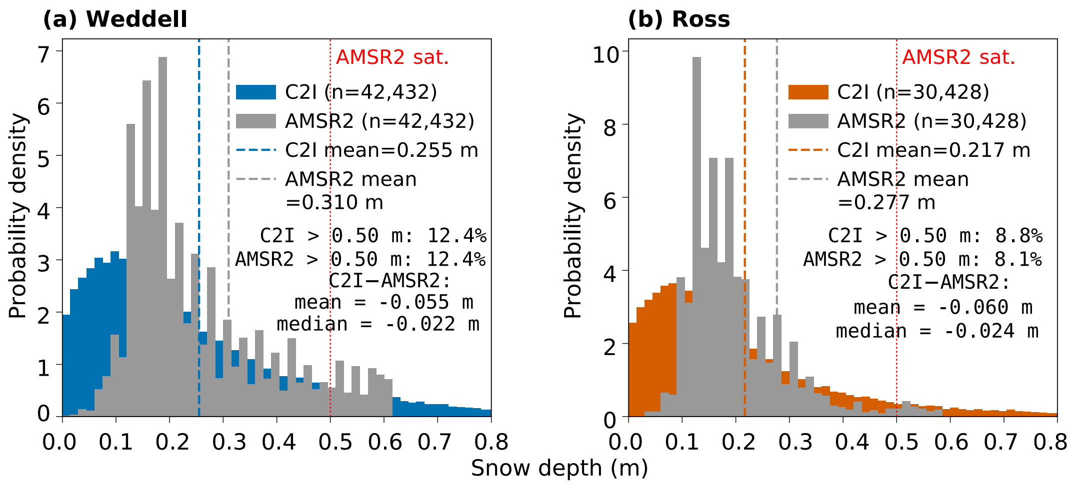

Figure 7. Normalized probability density distributions of CRYO2ICE (C2I) snow thickness (filled histograms) and Advanced Microwave Scanning Radiometer 2 (AMSR2) snow depth (step-line histograms) for the (a) Weddell Sea and (b) Ross Sea during the austral winter (May–October, 2022–2025). Vertical dashed lines mark the median of each distribution. The red dotted line at 0.50 m indicates the approximate saturation threshold of the AMSR2 algorithm (Markus & Cavalieri, 2009). Annotation boxes report the fraction of each product exceeding this threshold and the median C2I–AMSR2 bias.

To examine the spatial structure of the C2I–AMSR2 disagreement, we gridded both products on to a common 25 km polar stereographic grid (3,650 filled cells) and computed the per-cell mean difference (Figure 4). The Weddell Sea shows a mean cell-level bias of −0.055 m (median −0.026 m), with 60% of grid cells recording thicker AMSR2 than C2I snow depth. The Ross Sea shows a mean cell-level bias of −0.055 m (median −0.013 m), with AMSR2 exceeding C2I in 55% of grid cells. Within the Weddell Sea, the spatial pattern is non-uniform. The western sub-region (west of 45°W) shows the strongest negative bias, where thick MYI carries deep snowpacks that approach or exceed the effective saturation threshold of the AMSR2 algorithm (Markus & Cavalieri, 1998; Rostosky et al., 2018). The eastern Weddell Sea and the Ross Sea sub-regions, by contrast, show near-zero cell-level differences that are comparable to the per-matchup precision reported in Section 4.4.

Despite the systematic negative bias, the spatial distributions of C2I and AMSR2 snow depth are broadly consistent (Figure 4): both products independently show thicker snow in the western Weddell Sea than in the eastern Weddell Sea, and both show the Ross Sea as more spatially uniform with thinner snow. This intra-sector spatial agreement strengthens the conclusion that the retrieval captures real geophysical gradients in snow thickness, even where absolute magnitudes disagree.

The monthly time series of sector-mean C2I and AMSR2 snow depth (Figure 8) reveals that both products track the progressive snow accumulation from May to October in each sector, but AMSR2 consistently reports thicker snow throughout the winter. The C2I–AMSR2 offset varies substantially with month, suggesting a systematic measurement difference rather than a seasonally-modulated retrieval artifact. The IQR of AMSR2 is narrower than that of C2I, consistent with the coarser effective resolution of the passive-microwave product smoothing the spatial variability that the along-track altimetric retrieval resolves.

The probability density distributions (Figure 7) further characterize the structural differences between the two products. In the Weddell Sea, 12.4% of C2I retrievals and 12.4% of AMSR2 values exceed 0.50 m, while in the Ross Sea the corresponding fractions are 8.8% and 8.1%. The similar upper-tail fractions indicate that the C2I–AMSR2 bias is not driven primarily by AMSR2 saturation at thick snow depths; rather, the AMSR2 distribution is shifted toward thicker values across the full depth range relative to C2I. At the opposite end of the distribution, the passive-microwave retrieval is expected to under-represent the thinnest snow, because the gradient-ratio algorithm loses sensitivity as snow depth approaches zero. AMSR2 therefore captures fewer of the shallow values that C2I records, which contributes to the relative shift toward thicker AMSR2 depths and is consistent with the reduced thin-snow sensitivity discussed below. This systematic offset is consistent with incomplete Ku-band penetration causing C2I to underestimate snow thickness uniformly, with AMSR2's own retrieval biases contributing to the disagreement at all depths. A balanced interpretation must weight the well-

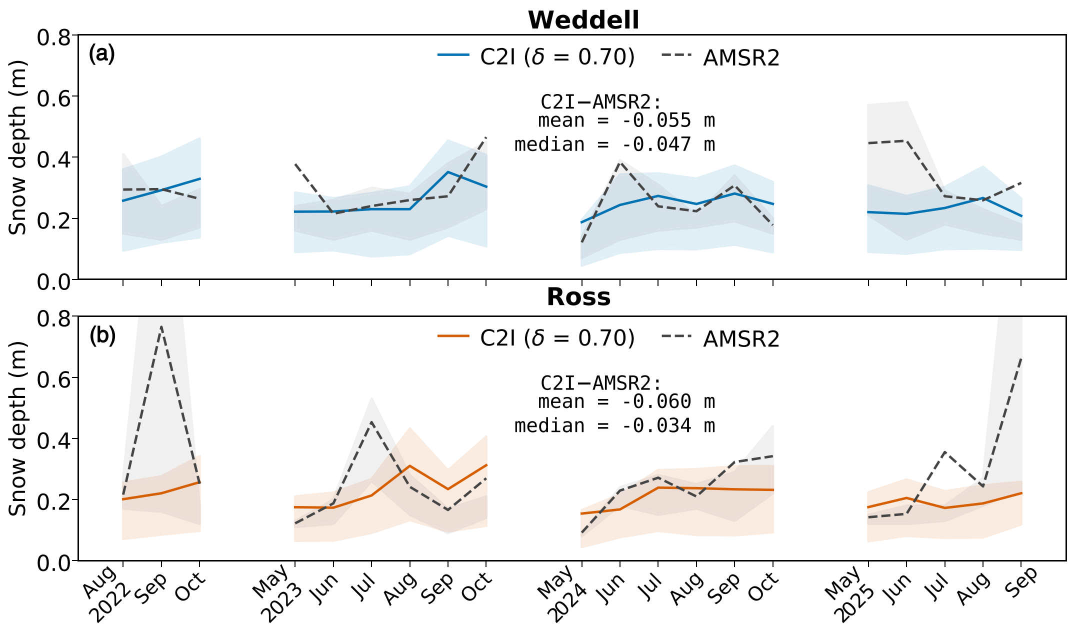

Figure 8. Monthly time series of sector-mean snow depth for CRYO2ICE (C2I; solid lines, with interquartile range (IQR) shading) and Advanced Microwave Scanning Radiometer 2 (AMSR2; dashed lines, with IQR shading) over four austral winters (2022–2025) for the (a) Weddell Sea and (b) Ross Sea. The C2I retrieval adopts $\delta = 0.70$. Both products track the progressive winter accumulation, with AMSR2 consistently reporting thicker snow depth. The mean and median C2I–AMSR2 bias are annotated in each panel.

documented limitations of the passive-microwave retrieval as heavily as those of the dual-altimetry retrieval. The AMSR2 algorithm has reduced sensitivity to thin snow and tends to saturate at depths approaching 0.50 m (Markus & Cavalieri, 1998; Rostosky et al., 2018); its brightness temperatures are affected by atmospheric water vapor and cloud liquid water; its coarse footprint mixes ice of different types, roughness, and open water within a single retrieval; and its empirical coefficients were developed primarily for Arctic conditions and are known to perform less reliably over the deformed and flooded snow regimes common in the Antarctic (Worby, Markus, et al., 2008; S. Kern & Ozsoy-Çiçek, 2016). The disagreement between the two products therefore reflects limitations on both sides, and neither should be regarded as a reference against which the other is validated.

Point-to-point correlations between C2I and AMSR2 snow thickness are low in both sectors (Weddell Sea: $r = 0.250$, $r^2 = 0.062$; Ross Sea: $r = 0.027$, $r^2 = 0.001$; Table 2, Figure 6). After correcting for along-track autocorrelation, the effective sample sizes reduce to $n_{\text{eff}} = 17{,}743$ (Weddell Sea) and $n_{\text{eff}} = 12{,}512$ (Ross Sea), and both correlations remain formally significant (Weddell Sea: $p < 0.001$; Ross Sea: $p = 2.1 \times 10^{-3}$). However, the low r^2 values indicate that the two products share little retrieval-scale variability, reflecting a fundamental disagreement that extends beyond the different effective resolutions (C2I ~ 5 km vs. AMSR2 12.5 km grid from 5-day averaged brightness temperatures) to the underlying measurement physics. In both sectors, the low r^2 indicates that AMSR2 explains essentially none of the retrieval-scale variability, and we do not attach interpretive weight to the marginally higher Weddell Sea value; the formal significance reflects the large sample size rather than a physically meaningful point-scale correspondence. The robust outcome of this comparison is not quantitative point-scale agreement, which is not expected given the differing measurement physics and spatial support, but the independent reproduction of the same large-scale regional ordering by two methods with unrelated error sources.

Despite the low point-to-point correlations and the negative median bias, both products independently confirm a Weddell–Ross sector contrast of similar magnitude (Table 2): AMSR2 shows a 0.057 m mean sector difference and C2I shows a 0.040 m mean sector difference. The two products reproduce the same sector ordering at aggregated scales, despite weak retrieval-scale covariance and different absolute distributions. This agreement is a regional consistency result, not an independent validation of either product or proof that the contrast is free of retrieval artifacts. The systematic negative C2I bias relative to AMSR2 is consistent with incomplete Ku-band

Table 3
Sensitivity of Retrieved Snow Thickness to the Assumed Radar Penetration Factor δ

	Weddell		Ross		Bias versus AMSR2				Weddell–Ross contrast	
					Mean		Median			
δ	Mean (m)	Median (m)	Mean (m)	Median (m)	Weddell	Ross	Weddell	Ross	Mean (m)	Median (m)
0.5	0.357	0.263	0.304	0.219	+0.047	+0.027	+0.020	+0.021	0.054	0.045
0.6	0.298	0.219	0.253	0.182	−0.012	−0.024	−0.019	−0.012	0.045	0.037
0.7[a]	0.256	0.188	0.216	0.155	−0.055	−0.060	−0.047	−0.034	0.038	0.032
0.8	0.223	0.165	0.190	0.137	−0.087	−0.087	−0.067	−0.050	0.033	0.028
0.9	0.198	0.146	0.169	0.121	−0.112	−0.108	−0.083	−0.063	0.030	0.025
1.0	0.179	0.132	0.152	0.109	−0.132	−0.125	−0.095	−0.073	0.027	0.022

Note. Both mean and median are reported to characterize the right-skewed distribution. The adopted baseline is $\delta = 0.70$, reflecting the literature consensus of 60%–90% Ku-band penetration (Fredensborg Hansen et al., 2025a; Landy et al., 2026; Nab et al., 2024; Zhou et al., 2026a). [a]Baseline ($\delta = 0.70$, $\rho_s = 330$ kg m^{-3}, $\eta_s = 1.263$).

penetration into the snowpack ($\delta < 1$), the sensitivity to which is quantified in Section 4.6 and interpreted in the Discussion. We emphasize, however, that AMSR2 is not a reference here: its own documented limitations, including reduced sensitivity to thin snow, saturation at deeper snow, and the application of Arctic-derived coefficients over Antarctic ice, act to bias the AMSR2 depths in the opposite direction, so the observed offset reflects errors in both products rather than a deficiency of C2I alone.

4.6. Sensitivity to Radar Penetration Factor

To quantify the sensitivity of the retrieved snow thickness to the incomplete Ku-band penetration, we repeat the retrieval for penetration factors $\delta = 0.50$ to 1.00 in increments of 0.10, where $h_s(\delta) = \Delta f / (\delta \cdot \eta_s)$ and $\delta = 0.70$ recovers the adopted baseline (Table 3). The retrieved snow thickness scales inversely with δ: reducing δ from 1.00 to 0.50 approximately doubles the inferred snow thickness in both sectors (Table 3; Figure 9a).

The median C2I–AMSR2 bias crosses zero at $\delta^* \approx 0.55$, and the mean bias crosses zero at $\delta^* \approx 0.58$, with both crossings occurring simultaneously in the Weddell Sea and Ross Sea sectors (Figure 9b). We do not interpret this crossing as a validated Ku-band penetration depth, because AMSR2 is itself an uncertain passive-microwave retrieval rather than an independent ground-truth reference. Instead, the crossing is treated as an AMSR2-equivalent scaling that indicates the penetration factor required to make the sector-mean or sector-median C2I estimates numerically consistent with AMSR2 under the present retrieval assumptions. Read in this way, the $\delta^* \approx 0.55$ scaling implies that the effective Ku-band scattering horizon would lie approximately 55% of the snowpack depth below the air–snow interface to reproduce the AMSR2 sector medians, which is shallower than the 60%–90% penetration range reported by Landy et al. (2026) for the Arctic and consistent with the higher brine content of Antarctic FYI limiting Ku-band penetration more severely (Mallett et al., 2024; Nandan et al., 2017). The finding that partial penetration ($\delta < 1$) is required to reproduce an external reference is consistent with Nab et al. (2024), who similarly found that partial penetration was optimal across all TFMRA retracking thresholds when tuning Arctic CS2 ice thickness to inter-annual variability recorded by upward-looking sonar moorings.

The Weddell–Ross sector contrast is preserved at every δ value tested (Table 3; Figure 9c): the mean sector difference ranges from 0.054 m at $\delta = 0.50$ to 0.027 m at $\delta = 1.00$, and the baseline $\delta = 0.70$ yields a mean contrast of 0.038 m. This test quantifies the sensitivity of the absolute magnitude, not the robustness of the sector ordering to regime-dependent scattering. Because δ enters as a multiplicative factor on Δf, any uniform reduction in penetration scales both sectors equally, so the negative-retrieval fraction and the Pearson correlation with AMSR2 are likewise invariant to δ. The relative sector finding is therefore robust to the penetration assumption, even though the absolute snow-thickness magnitude depends sensitively on δ.

5. Discussion

We discuss the results in eight subsections. Section 5.1 interprets the Weddell–Ross sector contrast in the context of regional ice-type morphology, snow accumulation history, and deformation regimes. Section 5.2 examines the

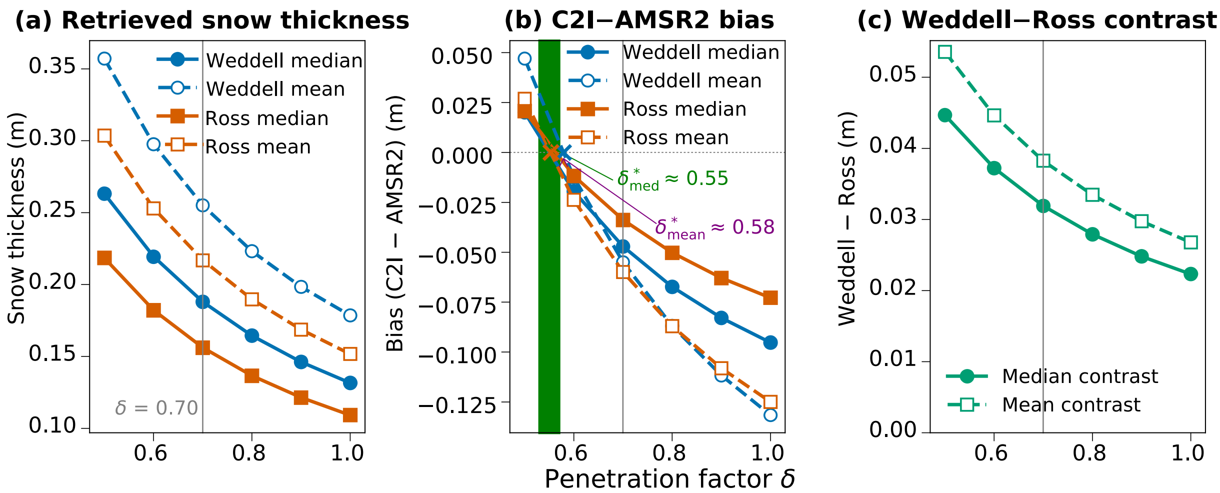

Figure 9. Sensitivity of retrieved snow thickness to the assumed radar penetration factor δ. (a) Retrieved snow thickness as a function of δ for the Weddell Sea (blue) and Ross Sea (orange); dashed lines with open markers show means, solid lines with filled markers show medians. (b) Mean and median CRYO2ICE (C2I)-Advanced Microwave Scanning Radiometer 2 (AMSR2) bias; the green band marks the optimal $\delta^* = 0.55$ where both sectors' median biases cross zero simultaneously. (c) Weddell–Ross contrast (mean and median difference).

implications of incomplete Ku-band penetration for the retrieval bias, and Section 5.3 interprets the persistent fraction of negative retrievals. Section 5.4 discusses the implications of the uncertainty budget for future retrievals, and Section 5.5 compares our results with prior Antarctic snow-thickness estimates. Section 5.6 then establishes the relationship between the C2I configuration and the upcoming CRISTAL mission, and Section 5.7 develops the implications of this study for CRISTAL retrieval design. Section 5.8 closes by enumerating the principal limitations of the present analysis.

5.1. Physical Drivers of the Weddell and Ross Seas Snow-Thickness Contrast

The observed Weddell–Ross contrast is consistent with known regional differences in ice age, ice thickness, snow accumulation history, and deformation regime, but the present analysis does not independently decompose these drivers. Accordingly, we interpret the sector contrast as a robust regional snow-thickness signal rather than as a direct attribution to any single physical mechanism. The ice-type composition of the two sectors differs fundamentally. The Weddell Sea is the primary Antarctic sector that retains appreciable MYI: the cyclonic Weddell Gyre transports ice westward from coastal formation zones and then northward along the Antarctic Peninsula, creating a pronounced age gradient from young FYI in the east to recirculated second-year and multi-year ice in the west (Massom et al., 2001; Melsheimer et al., 2023). Melsheimer et al. (2023) showed that nearly all Antarctic MYI is second-year ice that drifts to lower latitudes and melts within approximately 2 years, so that only ~15% of the circumpolar sea-ice cover survives any given summer. In the western Weddell Sea, the snowpack is older, deeper, and more metamorphosed, with mean bulk density of ~340 kg m^{-3} dominated by melt-freeze forms and depth hoar (Arndt et al., 2024, 2025). By contrast, the eastern Weddell Sea is dominated by seasonal FYI with thinner, younger snow at a lower mean density of ~264 kg m^{-3}, reflecting wind-slab and fragmented-grain stratigraphy under colder, drier conditions (Arndt et al., 2024, 2025). The Ross Sea differs from both Weddell Sea sub-regions: vigorous polynya-driven ice production exports predominantly thin FYI northward (Comiso et al., 2017; Koo et al., 2024; Tison et al., 2020), and although some MYI may persist in individual years, the Ross Sea is predominantly covered by seasonal FYI. The thinner ice reaches negative freeboard more readily, promoting snow–ice formation that converts accumulated snow into ice and limits the equilibrium snow depth, while katabatic winds from the continental interior fracture the thinner Ross Sea pack more readily and enhance snow loss from floe surfaces into leads (Itkin et al., 2023; Massom et al., 2001). These processes together produce the thinner, more spatially uniform snow cover evident in both the gridded retrievals (Figure 4) and the narrower Ross Sea probability density function (Figure 3a). This ice-type morphology has direct implications for both snow accumulation and Ku-band radar penetration: MYI sustains a deeper snowpack without conversion to snow ice, the contrasting penetration-limiting mechanisms over the two ice types are developed in Section 5.2.

The seasonal progression from May to October (Table C1; Figure 2) is consistent with progressive snow accumulation on an aging ice pack. Both sectors thicken through winter, but the Weddell Sea accumulates more snow in absolute terms (mean increase from 0.220 m in May to 0.309 m in September) than the Ross Sea (0.175 m in May to 0.265 m in October), consistent with the longer accumulation history on its older, thicker ice. The C2I retrievals also resolve intra-sector snow-thickness gradients that the gridded AMSR2 product does not capture (Figure 8): a decrease from the western toward the eastern Weddell Sea, and a gradient from the Ross Sea polynya toward the outer pack ice. This intra-sector resolution likely reflects both the finer along-track sampling of the C2I retrieval and the known limitations of the passive-microwave retrieval over heterogeneous ice surfaces.

5.2. Ku-Band Penetration and Implications for Retrieval Bias

In this study, we apply a penetration factor $\delta = 0.70$, reflecting the literature consensus that the CS2 Ku-band radar does not fully penetrate to the snow–ice interface (Arndt et al., 2024; Fredensborg Hansen et al., 2025b; Landy et al., 2026; Nab et al., 2024; Zhou et al., 2026a), so that the measured radar freeboard corresponds to the ice freeboard reduced by the snow-layer delay (Arndt et al., 2025). The mean C2I–AMSR2 biases are small and slightly positive in both sectors, whereas the median biases are negative (Table 2). Because both distributions are right-skewed, with a heavy upper tail in the C2I retrievals, the mean is pulled upward relative to the median; we therefore treat the median as the more representative descriptor of the typical matchup, and its negative sign indicates that the majority of matchups have C2I snow thickness lower than AMSR2 snow depth, as expected under incomplete Ku-band penetration. This negative median bias is consistent with incomplete penetration ($\delta < 1$): the radar scattering horizon lies within the snowpack rather than at the snow–ice interface, causing the retrieved snow thickness to be underestimated relative to the true value. Distinct physical mechanisms operate over FYI and MYI to produce this incomplete penetration.

Over FYI, brine wicking from the sea-ice surface into the basal snow layers increases the dielectric loss of the snow and creates a saline layer that can dominate the radar backscatter above the snow–ice interface (Geldsetzer et al., 2009; Nandan et al., 2017), while internal ice lenses formed by melt–refreeze cycles introduce additional scattering interfaces within the snowpack (Willatt et al., 2023). Over MYI, a different mechanism dominates: heavily-metamorphosed remnant snow layers with large sintered grains and superimposed ice at the base scatter Ku-band energy before it reaches the ice surface, even where basal salinity is low. Willatt et al. (2025) demonstrated this directly by deploying the surface-based KuKa polarimetric radar on five MYI floes in the Weddell Sea during the PS129 expedition (March–April 2022): the co-polarized Ku-band backscatter used by CS2 failed to detect the snow–ice interface beneath thick, metamorphosed remnant snow, with scattering instead occurring predominantly near the air–snow interface. Zhou et al. (2026b) provided complementary spaceborne evidence by decomposing Ku-band CS2 waveforms over the Weddell Sea into snow-surface, snow-volume, and ice-surface contributions; snow-volume scattering was comparable to or exceeded the ice-surface return under typical Antarctic conditions, confirming that the conventional assumption of dominant snow–ice interface scattering is frequently violated. The penetration-limiting mechanism therefore differs between FYI (brine-dominated) and MYI (metamorphism-dominated), with both leading to $\delta < 1$ for distinct physical reasons (Mallett et al., 2024).

The airborne validation of Fredensborg Hansen et al. (2025a) and Fredensborg Hansen et al. (2025b) over the Weddell Sea in December 2022 found that satellite-derived C2I snow thickness agreed with the airborne laser-ASIRAS Ku-band combination to within 0.03 m bias at 25 km scales. This validation was conducted during austral summer when wet-snow conditions further complicate Ku-band penetration. Our winter retrievals benefit from colder, drier snow conditions that should increase penetration relative to the summer case, yet the persistent negative bias against AMSR2 suggests that $\delta < 1$ remains relevant even during winter.

Our winter Antarctic results are consistent with recent Arctic findings that the Ku-band scattering horizon sits within rather than at the base of the snowpack during cold-season conditions. Taelman et al. (2026) tracked CS2 radar freeboards and IS2 laser freeboards over land-fast Arctic sea ice throughout the 2022 winter–summer cycle and found that, over FYI, the Ku-band radar freeboard tracks the snow–ice interface during most of the cold season (air temperatures below approximately -10°C). Over MYI, the scattering horizon was located at least 60% deep in the snowpack. Episodic positive biases in radar freeboard (under 4 cm) occurred during warming events and strong snowfall but accounted for only ~15% of the winter period. The relatively small magnitude of our negative C2I–AMSR2 median bias is consistent with deep but not complete penetration during cold austral winter conditions.

The adopted $\delta = 0.70$ represents a physically-motivated estimate within the literature range, and the penetration sensitivity analysis in Section 4.6 establishes the empirically optimal $\delta^* \approx 0.55$ that minimizes the median C2I–AMSR2 bias simultaneously in both sectors. Read as an AMSR2-equivalent scaling, this δ^* implies an effective Ku-band scattering horizon approximately 55% of the snowpack depth below the air–snow interface, which is shallower than the 60%–90% penetration range reported by Landy et al. (2026) for the Arctic but broadly consistent with the empirical finding of Taelman et al. (2026) that the scattering horizon over Arctic MYI lies at least 60% deep in the snowpack. The shallower Antarctic value is consistent with the higher brine content of Antarctic FYI limiting Ku-band penetration more severely than over Arctic ice (Mallett et al., 2024; Nandan et al., 2017), and with the finding of Nab et al. (2024) that partial penetration ($\delta < 1$) is optimal across all TFMRA retracking thresholds when Arctic CS2 ice thickness is tuned to upward-looking sonar mooring records. Crucially, incomplete penetration affects the absolute magnitude of the retrievals but not the relative sector contrast: because δ enters as a multiplicative factor on the freeboard difference, any uniform reduction in δ scales both sectors equally and preserves the Weddell–Ross difference established in Section 4.5.

5.3. Interpretation of Negative Snow-Thickness Retrievals

The observed 11%–12% fraction of negative retrievals is consistent with prior C2I studies: Fredensborg Hansen et al. (2024) reported a comparable fraction in the Arctic, and Kacimi and Kwok (2020) noted analogous behavior in their Antarctic gridded IS2–CS2 snow-thickness maps. This fraction should not be interpreted as evidence for physically negative snow thickness; rather, it occurs where the freeboard difference is small relative to the combined effects of measurement noise, collocation mismatch, residual surface-type errors, and unresolved sub-footprint heterogeneity. Retaining rather than truncating small negative values avoids imposing an artificial positive bias on sector means and distributional statistics. The negative fraction is invariant across all tested values of δ (Section 4.6), confirming that incomplete penetration alone cannot explain the negative retrievals: they arise primarily from irreducible measurement noise in Δf that is symmetric around the true value.

5.4. Implications of the Uncertainty Budget

The dominance of CS2 radar freeboard uncertainty in the per-matchup error budget (Section 4.4) has a direct practical implication: the most effective path to lower retrieval uncertainty is improved CS2 retracking precision rather than improved snow-density climatologies or refined permittivity formulations. This precision can be achieved through physically-based retracking algorithms that better resolve the snow–ice interface (Fredensborg Hansen et al., 2025b; Zhou et al., 2026a) or through multi-look averaging that reduces speckle noise at the cost of along-track resolution. The IS2 freeboard uncertainty is the second-largest component and is well characterized by the ATL10 product-level uncertainty propagation (Kwok et al., 2025), while the snow-density (refractive-index) term is the smallest contributor for the majority of retrievals and becomes significant only for the thickest snow ($h_s > 0.3$ m), where it contributes approximately 0.005 m. The insensitivity of the retrieval to the choice between the Tiuri et al. (1984)'s and Ulaby et al. (1986)'s permittivity formulations (less than 2% difference) confirms that the permittivity model is not a meaningful source of uncertainty at the current level of measurement noise.

The sector-independent mean per-matchup uncertainty of 0.040 m (Weddell Sea) and 0.039 m (Ross Sea) represents 20%–25% of the sector means and medians (Table C1). Because adjacent matchups share overlapping collocation windows, statistical significance is not assessed using the nominal matchup count; the autocorrelation-adjusted effective sample sizes (Table 1) provide a conservative first-order correction. For the sector-median test, the effective sample sizes are $n_{\text{eff}} = 20{,}948$ (Weddell Sea, 44% of $n = 47{,}735$) and $n_{\text{eff}} = 15{,}187$ (Ross Sea, 44% of $n = 34{,}606$); the AMSR2 correlation p-values reported in Table 2 use the corresponding values for the smaller comparison subset ($n_{\text{eff}} = 17{,}743$ Weddell Sea, $12{,}512$ Ross Sea). The resulting standard errors of the sector medians are of order 10^{-3} m, so the 0.038 m Weddell–Ross mean difference is resolved with high statistical confidence (contrast-to-standard-error ratio of 17.0) despite the per-retrieval noise. Even so, the effective sample size remains an approximate correction because the retrievals are not point samples at the native CS2 posting interval; we therefore emphasize the persistence of the Weddell–Ross contrast across months, years, density assumptions, penetration factors, and the independent AMSR2 product rather than relying primarily on formal *p*-values.

5.5. Comparison With Published Antarctic Snow-Thickness Estimates

The values reported here can be compared with prior observational estimates from independent methods, although direct comparisons are complicated by differences in sampling strategy, spatial scale, and ice-type coverage. At a high level, our C2I retrievals exceed the ASPeCt ship-based climatology by a factor of 1.5–3 (reflecting contrasting sampling biases), are broadly consistent in magnitude with the gridded pan-Antarctic retrievals of Kacimi and Kwok (2020) and the along-track Weddell Sea retrievals of Fredensborg Hansen et al. (2025b) and Zhou et al. (2026a), and are thinner than AMSR2 passive-microwave estimates by 0.02–0.04 m in the median. This pattern is qualitatively consistent with the Arctic C2I–climatology offsets reported by Fredensborg Hansen et al. (2024). Detailed comparisons with each of these data sets are developed below.

The ASPeCt ship-based climatology (Worby, Geiger, et al., 2008) reports mean winter snow thickness of 0.08 m for the eastern Weddell Sea and 0.15 m for the Ross Sea (Table 3 of Worby, Geiger, et al. (2008)); no winter observations are available for the western Weddell Sea, where sea-ice conditions preclude ship access during winter. Our C2I eastern Weddell Sea sub-sector mean of 0.219 m (computed for matchups east of 45°W; Section 4.2) substantially exceeds the ASPeCt eastern Weddell Sea mean of 0.08 m, although the comparison is complicated by contrasting sampling strategies. Our along-track satellite retrieval covers the full ice-covered area including deformed ice, whereas the ASPeCt ship-based protocol preferentially samples level ice in navigable waters (Williams et al., 2015; Worby, Markus, et al., 2008); both biases act to underestimate the true area-averaged snow thickness reported by ASPeCt. The Ross Sea comparison shows a similar pattern: our C2I Ross Sea mean of 0.217 m exceeds the ASPeCt Ross Sea mean of 0.15 m. While the level-ice sampling preference of ASPeCt is well-documented for sea-ice thickness (Williams et al., 2015; Worby, Markus, et al., 2008), its effect on snow thickness is less clearly characterized; the offset between our along-track satellite retrievals and the ASPeCt snow-thickness climatology may also reflect genuine differences between the 2004–2007 period covered by ASPeCt and the 2022–2025 period covered here.

The AMSR2 product samples the entire ice-covered area without this spatial sampling bias, but its retrieval degrades substantially over rough and deformed ice where surface roughness alters the passive-microwave emissivity (Worby, Markus, et al., 2008; S. Kern & Ozsoy-Çiçek, 2016). The two products therefore carry fundamentally different biases that should not be conflated.

Our C2I retrievals sample along the satellite ground tracks without a priori discrimination between level and deformed ice, and therefore capture both smooth and rough ice contributions to the snow-thickness distribution. This represents an important difference in sampling strategy relative to both the ship-based and passive-microwave approaches.

Kacimi and Kwok (2020) retrieved circumpolar-Antarctic snow thickness from gridded IS2 and CS2 freeboards in 2019 using the same permittivity formulation adopted here. Their Table 2 reports Ross Sea winter snow of approximately 0.07–0.12 m, whereas our Ross Sea monthly means range from approximately 0.16–0.30 m (medians 0.12–0.20 m; Figure 2, Table C1) across the winter months at the baseline $\delta = 0.70$. Three candidate explanations are consistent with this difference. First, the two studies cover different periods (2019 vs. 2022–2025), and genuine inter-annual variability in the Ross Sea accumulation cannot be excluded. Second, the studies adopt different penetration assumptions, and our own sensitivity analysis (Section 4.6) shows that increasing δ toward unity reduces our Ross Sea estimate substantially, bringing it closer to the values of Kacimi and Kwok (2020); the difference is therefore partly a consequence of the penetration assumption rather than a discrepancy in the underlying freeboards. Third, the gridded monthly approach of Kacimi and Kwok (2020) averages over a 25 km grid, whereas our along-track collocation samples at finer scale and retains deformed-ice contributions that a coarser grid may smooth. The Weddell Sea comparison is more nuanced, because Kacimi and Kwok (2020) resolve the sector into western and eastern sub-regions: their Table 2 reports a western (multi-year) Weddell Sea snow depth of approximately 0.20–0.23 m and an eastern (first year) value of approximately 0.08–0.15 m, against our combined Weddell Sea mean of 0.255 m at $\delta = 0.70$. Our estimate lies closest to their western multi-year values, and the same period, penetration, and gridding considerations apply, with a higher penetration factor again reducing our estimate toward theirs. Zhou et al. (2026a) derived along-track snow depth from 46 C2I tracks over the Weddell Sea during 2020–2022 using an optimized TFMRA-70 retracker and

10.1029/2026EA005247

validated these retrievals against snow buoy observations. Their Weddell Sea snow depths are broadly consistent with our Weddell Sea retrievals, though a direct comparison is complicated by the different CS2 retracking methodology (TFMRA-70 vs. Baseline-E), the earlier study period (2020–2022 vs. 2022–2025), and differences in the IS2 product used (ATL07 vs. ATL10). Notably, Zhou et al. (2026a) also found substantial discrepancies between different CS2 processing chains, reinforcing our finding (Section 5.8) that the sensitivity of Antarctic C2I retrievals to the choice of retracker remains a key source of uncertainty.

The Cryo2IceEx/DEFIANT airborne campaign (Fredensborg Hansen et al., 2025a, 2025b) reported C2I snow thickness over the Weddell Sea in December 2022, providing the only independent evaluation of the spaceborne C2I retrieval over Antarctic sea ice. Their summer values are not directly comparable to our winter retrievals, but the seasonal cycle implied by our May-October progression (Table C1) is consistent with thinner summer snow following the spring-summer melt.

The AMSR2 benchmarking (Section 4.5) provides further independent context. The residual C2I–AMSR2 disagreement (small positive mean biases; median biases −0.015 to −0.012 m) is consistent with the known tendency of the LaKu approach to underestimate snow thickness under incomplete penetration, while the AMSR2 algorithm may overestimate snow depth over deformed ice where volume scattering is enhanced (Rostosky et al., 2018). The pattern of lower altimetric estimates relative to passive-microwave snow depth and limited point-to-point agreement $\left(r^2 \leq 0.062\right)$ is not unique to this study: Fredensborg Hansen et al. (2024) found qualitatively similar behavior in their Arctic C2I analysis (winter 2020–2022), where along-track C2I snow thickness was thinner than the climatology of Warren et al. (1999), yet both products captured the same large-scale spatial gradients. These findings collectively suggest that the LaKu approach resolves regional contrasts robustly even when absolute magnitudes carry significant uncertainty, a pattern that appears consistent across both hemispheres and multiple independent studies. The C2I–AMSR2 comparison is therefore considered here as a mutual benchmarking exercise in which neither product represents ground truth.

5.6. Relationship Between C2I and Copernicus polaR Ice and Snow Topography ALtimeter (CRISTAL)

The C2I configuration is a methodological precursor for CRISTAL in the specific sense that both rely on differencing two co-located altimetric surfaces to retrieve snow depth along-track, and the collocation, retrieval, and uncertainty framework developed here transfers directly to CRISTAL. We stress that the frequency architectures differ: CRISTAL pairs Ka-band and Ku-band radars (M. Kern et al., 2020; Landy et al., 2026), whereas C2I pairs a laser with a Ku-band radar. Importantly, the Ka–Ku pairing does not by itself resolve the penetration ambiguity that limits the absolute magnitude in our retrieval, because the position of the dominant scattering horizon remains unknown at both frequencies; CRISTAL's principal advantage is improved same-orbit snow-depth sampling rather than a direct constraint on penetration. With that distinction in mind, our results inform CRISTAL in three ways, developed in the following subsection.

5.7. Implications of This Study for CRISTAL Retrieval Design

The collocation, retrieval, and uncertainty results presented above translate into three concrete implications for CRISTAL. First, although the formal per-matchup precision is dominated by instrument noise and is essentially sector-independent (Section 3.4), the systematic component of the retrieval, set by the depth of the Ku-band scattering horizon, is strongly sector-dependent. It is this systematic, sector-dependent penetration behavior, rather than the random precision, that motivates region-specific CRISTAL retrievals: the sector-dependent snow conditions documented here suggest that CRISTAL retrieval algorithms should be evaluated regionally rather than assuming uniform performance across the Antarctic, since the brine-driven and metamorphism-driven penetration regimes we identify over FYI and MYI will affect the Ka and Ku channels differently (Nandan et al., 2017; Willatt et al., 2025). The evidence that co-polarized Ku-band returns over Antarctic MYI can scatter near the air–snow interface (Willatt et al., 2025; Zhou et al., 2026b) implies that a Ka–Ku retrieval will retain a residual scattering-horizon ambiguity, and that an independent laser reference of the kind exploited here would remain valuable for constraining it.

Second, the uncertainty budget established here provides a template for CRISTAL error decomposition. Our finding that CS2 radar freeboard dominates the error budget suggests that the improved along-track resolution and reduced speckle noise expected from CRISTAL's Ku-band altimeter (M. Kern et al., 2020) could substantially reduce the per-retrieval uncertainty relative to the current C2I configuration.

Third, the analysis uses a single CS2 retracker product (Baseline-E). Both Fredensborg Hansen et al. (2025b) and Zhou et al. (2026a) demonstrated that the choice of Ku-band waveform retracking methodology significantly affects the retrieved snow thickness; Zhou et al. (2026b) further showed that snow-volume scattering can dominate the Ku-band waveform under Antarctic conditions, meaning that the effective scattering horizon assumed by different retrackers may vary substantially. The sensitivity of our Antarctic results to alternative retrackers has not been assessed.

Looking further ahead, the proposed Earth Dynamics Geodetic Explorer (EDGE) mission (Garvin et al., 2026) would pair a multi-beam laser with operational Ku-band radars to extend along-track dual-altimetry sampling well beyond the current C2I configuration. The sector-dependent snow conditions and uncertainty budget established here provide a baseline against which both CRISTAL and future EDGE-based retrievals can be evaluated.

5.8. Limitations

The present analysis is subject to several limitations that should be considered when interpreting the results and applying them to downstream applications.

No explicit sea-ice concentration (SIC) filter is applied to the matchups, so observations near the sea-ice edge or over low-concentration areas may include mixed ice–ocean surfaces that bias freeboard estimates, despite the quality-control filters applied to both ATL10 and CS2 surface-type classifications. However, these existing quality-control filters effectively exclude most marginal-ice-zone observations: the mean AMSR2-derived SIC at each matchup location is 99.4% (median 100%), and only 0.3% of winter matchups fall below 80% SIC (223 of 82,341; Appendix B). Repeating the analysis after excluding matchups with SIC below 80% removes fewer than 0.3% of observations per sector, leaves the sector medians unchanged to three decimal places (Weddell Sea 0.188 m; Ross Sea 0.156 m), and preserves the Weddell–Ross sector median contrast at 0.032 m (Appendix B). Even at the stricter 90% threshold, the results are indistinguishable from the baseline, confirming that low-concentration contamination does not affect the reported sector contrasts.

The two altimeters observe overlapping but not identical sea-ice areas: even in the absence of sea-ice drift, the 1.6 km cross-track width of the CS2 SAR-mode swath means that CS2 and IS2 never measure exactly the same sea-ice surface, introducing irreducible representativeness noise in the freeboard difference. Sea-ice drift during the <4 hr coincidence interval adds a further displacement of order 0.5 km, which is small relative to the 5 km collocation radius but contributes additional noise for individual matchups.

The retrieval adopts a single CS2 retracker product (Baseline-E), and the sensitivity to alternative retracking methodologies, which Fredensborg Hansen et al. (2025b) and Zhou et al. (2026a) have shown can substantially affect the retrieved snow thickness, represents an important avenue for future investigation. The CS2 radar freeboard uncertainty is set to a constant 0.030 m per 20-Hz measurement because the Baseline-E product does not provide a per-measurement retracking uncertainty; this constant value is a deliberately conservative estimate of combined instrument and retracking noise. A direct consequence is that the matchup-to-matchup variability in the total per-matchup precision (Equation 6) is carried almost entirely by the IS2 term, whose product-reported segment uncertainties vary with photon-counting statistics and sea-surface reference quality, while the CS2 term contributes a near-constant floor. A spatially varying CS2 retracking uncertainty would be preferable but is not available from the current product, and we report the relative magnitudes of the two terms so that readers can see the IS2 term governs the spatial structure of the precision. More fundamentally, the assumed Ku-band penetration factor ($\delta = 0.70$) is applied uniformly across all matchups and both sectors; Taelman et al. (2026) showed that Ku-band penetration varies episodically with snow temperature, salinity (brine volume >1%), and recent snowfall, introducing transient biases of up to 4 cm during winter that our uniform δ does not capture. While the penetration sensitivity analysis (Section 4.6) demonstrates that the sector contrast is insensitive to δ, the along-track variability of the effective scattering horizon remains unquantified.

The analysis is restricted to austral winter (May–October) when the dry-snow assumption underlying the refractive-index correction is best satisfied; extension to shoulder seasons and austral summer would require corrections for wet-snow conditions that are beyond the scope of this study (Fredensborg Hansen et al., 2025b; Willatt et al., 2023, 2025; Zhou et al., 2026a). Furthermore, the ground-based Weddell Sea observations of Willatt et al. (2025) indicate that even during the cold season, the effective Ku-band penetration depth may differ between

FYI and MYI due to distinct snow metamorphism regimes, suggesting that ice-age-dependent δ calibrations may improve future retrievals. Finally, no direct in situ validation has yet been conducted for the retrieved snow-thickness values; the AMSR2 comparison provides mutual benchmarking against an independent product rather than validation against a known reference. Dedicated field campaigns with coincident ground-based snow measurements, such as future extensions of the Cryo2IceEx program, would be required for formal validation of the absolute snow-thickness magnitudes reported here.

6. Conclusions

This study presents multi-winter along-track C2I snow-thickness estimates over the Weddell and Ross Sea sectors from 82,341 winter matchups between IS2 and CS2 during August 2022 to September 2025. Its central contribution is not the regional contrast itself, which is broadly expected from the contrasting ice regimes of the two sectors, but the systematic characterization of which features of along-track Antarctic dual-altimetry retrieval are robust and which are not, together with a quantification of the sensitivity of the absolute snow thickness to the unresolved Ku-band scattering horizon. The most robust empirical result is a persistent Weddell–Ross sector contrast that is invariant to the retrieval assumptions: Weddell Sea winter snow thickness exceeds that of the Ross Sea by 0.038 m in the mean (0.255 vs. 0.217 m) and by 0.032 m in the median (0.188 vs. 0.156 m), and the contrast persists across months, years, snow-density assumptions, and tested Ku-band penetration factors. The AMSR2 passive-microwave snow-depth product independently reproduces the same sector ordering, with a 0.057 m mean sector difference, although the two products exhibit weak point-to-point agreement $\left(r^2 \leq 0.062\right)$ and structurally different distributions at the retrieval scale.

The formal propagated precision of the C2I estimates is 0.040 m per matchup in the Weddell Sea and 0.039 m in the Ross Sea, dominated by the assumed CS2 radar-freeboard uncertainty rather than by the snow-density or permittivity assumptions. The absolute snow-thickness magnitude nevertheless remains sensitive to the unresolved Ku-band scattering horizon, the choice of CS2 retracker, and the absence of coincident in situ validation. The present data set therefore constitutes a multi-year along-track regional and seasonal benchmarking product for evaluating the relative structure of Antarctic snow thickness, rather than a fully validated absolute snow-depth record.

These results support the use of along-track dual-altimetry observations for resolving regional and seasonal Antarctic snow-thickness contrasts and provide a practical framework for evaluating future retrievals from the upcoming CRISTAL mission. The penetration sensitivity analysis further establishes that the AMSR2 sector medians can be reproduced by an effective Ku-band penetration factor of $\delta^* \approx 0.55$, which we interpret as an AMSR2-equivalent scaling rather than a validated penetration depth. The substantial retrieval-scale disagreement between AMSR2 snow depth and dual-altimetry snow thickness, despite their concordant sector ordering, demonstrates that the two products cannot be treated as interchangeable inputs for hydrostatic sea-ice-thickness conversion at the matchup scale; the resulting ice-thickness retrievals will inherit the choice of snow-depth product as a structural systematic, with implications for any snow-thickness comparison that mixes these products.

Acronyms

AMSR	Advanced Microwave Scanning Radiometer
ASPeCt	Antarctic Sea Ice Processes and Climate
C2I	CRYO2ICE
CDF	Cumulative Distribution Function
CS2	CryoSat-2
EDGE	Earth Dynamics Geodetic Explorer
ESA	European Space Agency
FYI	First Year Ice
IDW	Inverse-Distance Weighting

IS2	ICESat-2
LaKu	Laser–Ku-Band
MYI	Multi-Year Ice
NASA	National Aeronautics and Space Administration
NSIDC	National Snow and Ice Data Center
SAR	Synthetic Aperture Radar
SIRAL	SAR Interferometric Radar Altimeter
SIC	Sea-Ice Concentration
TFMRA	Threshold First-Maximum Retracker Algorithm

Appendix A: Snow-Density Sensitivity Tests

This appendix quantifies the sensitivity of the retrieved snow thickness to the assumed snow density and to the choice of dry-snow permittivity formulation, supporting the robustness claims made in Section 4.4 of the main text. Varying the assumed snow density across the plausible Antarctic range of $\rho_s = 260$, 330, and 400 kg m^{-3} (Massom et al., 2001; Sturm & Massom, 2017) changes the retrieved mean snow thickness by 0.023 m in the Weddell Sea (0.244–0.267 m) and by 0.020 m in the Ross Sea (0.207–0.227 m), as reported in Table A1. Both ranges are smaller than the mean per-matchup precision of 0.040 m established in Table C1 of the main text.

The Weddell–Ross sector contrast is preserved at every density tested, with mean differences of 0.037–0.040 m across the full density range, confirming that the sector contrast is insensitive to the assumed snow density (Table A1).

A separate test addresses the dry-snow permittivity formulation. Substituting the Tiuri et al. (1984) permittivity $\left(\varepsilon' = 1 + 1.7\,\rho_s + 0.7\,\rho_s^2\right)$ for the Ulaby et al. (1986) parameterization used in the baseline retrieval changes the retrieved snow thickness by less than 2%, which is negligible relative to the per-matchup precision of 0.040 m and confirms that the choice of permittivity model is not a meaningful source of uncertainty at the current measurement-noise level.

Table A1
Sensitivity of Retrieved Snow Thickness to the Assumed Snow Density ρ_s Across the Plausible Antarctic Range

		Weddell sea		Ross sea	
ρ_s (kg m^{-3})	η_s	Mean (m)	Median (m)	Mean (m)	Median (m)
260	1.205	0.267	0.197	0.227	0.164
330[a]	1.263	0.255	0.188	0.217	0.156
400	1.321	0.244	0.180	0.207	0.149

Note. Mean and median are reported in each sector to characterise the right-skewed distribution. The refractive index η_s is computed from ρ_s via Equation 5 of the main text. The baseline density is $\rho_s = 330$ kg m^{-3}. [a]Baseline snow density adopted in the main analysis.

Appendix B: Sea-Ice Concentration Sensitivity Test

This appendix tests whether the absence of an explicit SIC filter affects the reported results, supporting the robustness claim in Section 5.8. The AMSR2-derived SIC at the 82,341 winter matchups is strongly concentrated at high values (mean 99.4%, median 100%), with only 0.3% of matchups below 80% SIC and more than 99% at or above 90% in both sectors. Re-running the analysis at 80% and 90% SIC thresholds leaves the sector means, medians, per-matchup precision, AMSR2 bias, and Weddell–Ross contrast unchanged to three decimal places

(Table B1). The existing ATL10 and CS2 surface-type and freeboard-range filters therefore act as an effective SIC filter, and low-concentration contamination does not materially affect any reported result.

Table B1
Sensitivity of Key Results to Sea-Ice Concentration (SIC) Filtering

SIC filter	Sector	n	$n_{h_s>0}$	Neg. (%)	Mean h_s (m)	Median h_s (m)	Bias (m)	r
Baseline	Weddell	47,735	42,447	11.1	0.255	0.188	−0.047	0.250
	Ross	34,606	30,460	12.0	0.217	0.156	−0.034	0.027
≥80%	Weddell	47,602	42,342	11.0	0.255	0.188	−0.047	0.250
	Ross	34,516	30,390	12.0	0.217	0.156	−0.033	0.027
≥90%	Weddell	47,580	42,323	11.0	0.255	0.188	−0.047	0.250
	Ross	34,407	30,307	11.9	0.217	0.156	−0.033	0.027

Note. The baseline analysis applies no explicit SIC filter. Values are computed over all winter (May–October) matchups in the Weddell Sea and Ross Sea sectors. Bias is defined as CRYO2ICE (C2I) minus Advanced Microwave Scanning Radiometer 2 (AMSR2; median). r is the Pearson correlation between C2I and AMSR2 snow depth. Weddell–Ross mean contrast: Baseline = 0.038 m; SIC ≥ 80% = 0.038 m; SIC ≥ 90% = 0.038 m.

Appendix C: Monthly Snow-Thickness Summary Statistics

This appendix reports the full monthly summary statistics of retrieved snow thickness by sector (Table C1), comprising the overall winter statistics and the month-by-month progression of the median and the mean with its autocorrelation-adjusted standard error. The monthly means and medians are shown graphically in Figure 2 of the main text.

Table C1
Summary of CRYO2ICE Matchup Yield and Retrieved Snow-Thickness Statistics for the Austral Winter (May–October, 2022–2025), Stratified by Sector

	Weddell sea	Ross sea
Winter matchups	47,735	34,606
Valid $h_s > 0$ (%)	88.9	88.0
Negative $h_s \leq 0$ (%)	11.1	12.0
Mean h_s (m)	0.255	0.217
Median h_s (m)	0.188	0.156
Std. dev. h_s (m)	0.233	0.210
IQR h_s (m)	0.097–0.339	0.081–0.277
Mean σ_{h_s} (m)	0.040	0.039
Median σ_{h_s} (m)	0.038	0.038
Monthly median (mean ± standard error) h_s (m)		
May	0.169 (0.220 ± 0.003)	0.120 (0.175 ± 0.005)
June	0.164 (0.228 ± 0.005)	0.138 (0.185 ± 0.003)
July	0.174 (0.248 ± 0.006)	0.168 (0.219 ± 0.004)
August	0.185 (0.249 ± 0.003)	0.156 (0.221 ± 0.004)
September	0.236 (0.309 ± 0.005)	0.162 (0.228 ± 0.005)
October	0.219 (0.296 ± 0.007)	0.198 (0.265 ± 0.005)

Note. The upper panel reports overall winter statistics; the lower panel shows the monthly progression of median as well as mean plus and minus standard error of snow thickness.

Conflict of Interest

The authors declare no conflicts of interest relevant to this study.

Availability Statement

All the data sets and software used in this study are publicly available. AMSR2: https://nsidc.org/data/au_si12/versions/1 (last access: February 2026; Meier et al. (2018)); ICESat-2 ATL10 version 7: https://nsidc.org/data/atl10/versions/7 (last access: February 2026; Kwok et al. (2025)); CryoSat-2 Baseline-E Level-2: ftp://science-pds.cryosat.esa.int (last access: February 2026; European Space Agency (2021b)); Code and derived data sets used in this project are publicly available on Zenodo via https://doi.org/10.5281/zenodo.19220192 (Liu, 2026).

Acknowledgments

XL acknowledges support from the CoSE Tasmania Graduate Research Scholarship and Australian Antarctic Program Partnership (AAPP) Top-up Scholarship. This research was undertaken with the assistance of resources from the National Computational Infrastructure (NCI Australia), an NCRIS enabled capability supported by the Australian Government, through project gv90. pH, SC, RT, and ADF acknowledge support from the Australian Antarctic Science Program (AAS4625) and pH also those of AAS4496 and AAS4506. pH & RT are supported through grant funding from the International Space Science Institute (Switzerland; ISSI; Project 501). ADF is supported by the Australian Research Council, through grants FT230100234, LP170101090, LE220100103 and DP240100325. ADF acknowledges the generous support of the Harris Charitable Trust through the Antarctic Science Foundation. This work contributes to Project 6 of the Australian Antarctic Program Partnership (ASCI000002) funded under the Australian Government's Antarctic Science Collaboration Initiative program. We also thank Dr Robert A. Massom for providing valuable suggestions and feedback on revising and improving this manuscript. Open access publishing facilitated by University of Tasmania, as part of the Wiley - University of Tasmania agreement via the Council of Australasian University Librarians.

References

Arndt, S., Haas, C., Meyer, H., Peeken, I., & Krumpen, T. (2021). Recent observations of superimposed ice and snow ice on sea ice in the northwestern Weddell Sea. *The Cryosphere*, *15*(9), 4165–4178. https://doi.org/10.5194/tc-15-4165-2021

Arndt, S., Maaß, N., Rossmann, L., & Nicolaus, M. (2024). From snow accumulation to snow depth distributions by quantifying meteoric ice fractions in the Weddell Sea. *The Cryosphere*, *18*(4), 2001–2015. https://doi.org/10.5194/tc-18-2001-2024

Arndt, S., Webster, M., Sturm, M., & Massom, R. A. (2025). Snow on sea ice and how it varies through the seasons. In D. N. Thomas (Ed.), *Sea ice: Its physics, chemistry, biology, geology and societal importance* (4th ed., pp. 41–112). John Wiley & Sons Ltd. Retrieved from. https://doi.org/10.1002/9781394213764.ch02

Comiso, J. C., Gersten, R. A., Stock, L. V., Turner, J., Perez, G. J., & Cho, K. (2017). Positive trend in the Antarctic sea ice cover and associated changes in surface temperature. *Journal of Climate*, *30*(6), 2251–2267. https://doi.org/10.1175/jcli-d-16-0408.1

European Space Agency. (2021a). CryoSat-2 product handbook, baseline E 1.0 draft C, C2-LI-ACS-ESL-5319 [Data product user manual]. Retrieved from https://earth.esa.int/eogateway/documents/20142/0/CryoSat-Product-Handbook-Baseline-E-draft.pdf

European Space Agency. (2021b). Level 2 (L2) SAR precise orbit. Baseline E. [dataset]. European Space Agency. Retrieved from ftp://science-pds.cryosat.esa.int/

Fredensborg Hansen, R. M., Skourup, H., Rinne, E., Jutila, A., Lawrence, I. R., Shepherd, A., et al. (2025a). Multi-frequency altimetry snow depth estimates over heterogeneous snow-covered antarctic summer sea ice–part 1: C/S-Ku-and Ka-band airborne observations. *The Cryosphere*, *19*(10), 4167–4192. https://doi.org/10.5194/tc-19-4167-2025

Fredensborg Hansen, R. M., Skourup, H., Rinne, E., Høyland, K. V., Landy, J. C., Merkouriadi, I., & Forsberg, R. (2024). Arctic freeboard and snow depth from near-coincident CryoSat-2 and ICESat-2 (CRYO2ICE) observations: A first examination of winter sea ice during 2020–2022. *Earth and Space Science*, *11*(4), e2023EA003313. https://doi.org/10.1029/2023ea003313

Fredensborg Hansen, R. M., Skourup, H., Rinne, E., Jutila, A., Lawrence, I. R., Shepherd, A., et al. (2025b). Multi-frequency altimetry snow depth estimates over heterogeneous snow-covered Antarctic summer sea ice–part 2: Comparing airborne estimates with near-coincident CryoSat-2 and ICESat-2 (CRYO2ICE). *The Cryosphere*, *19*(10), 4193–4209. https://doi.org/10.5194/tc-19-4193-2025

Garvin, J. B., McDonagh-Smith, P., Peters, R. M., Fricker, H. A., Armston, J. D., Blair, J. B., & Luthcke, S. B. (2026). Return on investment and economic impact of a NASA-funded swath mapping laser altimeter orbiter for Earth surface elevations situational awareness in 2031–2040. *New Space*, *14*(2), 82–98. https://doi.org/10.1177/21680256261434504

Geldsetzer, T., Langlois, A., & Yackel, J. (2009). Dielectric properties of brine-wetted snow on first-year sea ice. *Cold Regions Science and Technology*, *58*(1–2), 47–56. https://doi.org/10.1016/j.coldregions.2009.03.009

Giles, K. A., Laxon, S. W., & Ridout, A. L. (2008). Circumpolar thinning of arctic sea ice following the 2007 record ice extent minimum. *Geophysical Research Letters*, *35*(22). https://doi.org/10.1029/2008gl035710

Guerreiro, K., Fleury, S., Zakharova, E., Rémy, F., & Kouraev, A. (2016). Potential for estimation of snow depth on Arctic sea ice from CryoSat-2 and SARAL/AltiKa missions. *Remote Sensing of Environment*, *186*, 339–349. https://doi.org/10.1016/j.rse.2016.07.013

Itkin, P., Hendricks, S., Webster, M., von Albedyll, L., Arndt, S., Divine, D., et al. (2023). Sea ice and snow characteristics from year-long transects at the MOSAiC central observatory. *Elementa: Science of the Anthropocene*, *11*(1), 00048. https://doi.org/10.1525/elementa.2022.00048

Kacimi, S., & Kwok, R. (2020). The Antarctic sea ice cover from ICESat-2 and CryoSat-2: Freeboard, snow depth, and ice thickness. *The Cryosphere*, *14*(12), 4453–4474. https://doi.org/10.5194/tc-14-4453-2020

Kacimi, S., & Kwok, R. (2022). Arctic snow depth, ice thickness, and volume from ICESat-2 and CryoSat-2: 2018–2021. *Geophysical Research Letters*, *49*(5), e2021GL097448. https://doi.org/10.1029/2021gl097448

Kern, M., Cullen, R., Berruti, B., Bouffard, J., Casal, T., Drinkwater, M. R., et al. (2020). The copernicus polar ice and snow topography altimeter (CRISTAL) high-priority candidate mission. *The Cryosphere*, *14*(7), 2235–2251. https://doi.org/10.5194/tc-14-2235-2020

Kern, S., & Ozsoy-Çiçek, B. (2016). Satellite remote sensing of snow depth on Antarctic sea ice: An inter-comparison of two empirical approaches. *Remote Sensing*, *8*(6), 450. https://doi.org/10.3390/rs8060450

Koo, Y., Xie, H., & Ackley, S. F. (2024). Thermodynamic and dynamic variations in sea ice thickness of the Ross Sea, Antarctica, driven by atmospheric circulation. *Journal of Geophysical Research: Oceans*, *129*(10), e2023JC020622. https://doi.org/10.1029/2023jc020622

Kwok, R., Kacimi, S., Webster, M., Kurtz, N., & Petty, A. (2020). Arctic snow depth and sea ice thickness from ICESat-2 and CryoSat-2 freeboards: A first examination. *Journal of Geophysical Research: Oceans*, *125*(3), e2019JC016008. https://doi.org/10.1029/2019jc016008

Kwok, R., & Maksym, T. (2014). Snow depth of the Weddell and Bellingshausen sea ice covers from IceBridge surveys in 2010 and 2011: An examination. *Journal of Geophysical Research: Oceans*, *119*(7), 4141–4167. https://doi.org/10.1002/2014JC009943

Kwok, R., Petty, A. A., Cunningham, G., Markus, T., Hancock, D., Ivanoff, A., et al. (2025). ATLAS/ICESat-2 L3A Sea Ice Freeboard, Version 7 [Dataset]. *NASA National Snow and Ice Data Center Distributed Active Archive Center*. https://doi.org/10.5067/ATLAS/ATL10.007

Landy, J. C., de Rijke-Thomas, C., Nab, C., Lawrence, I., Glissenaar, I. A., Mallett, R. D., et al. (2026). Anticipating CRISTAL: An exploration of multi-frequency satellite altimeter snow depth estimates over Arctic sea ice, 2018–2023. *The Cryosphere*, *20*(1), 183–208. https://doi.org/10.5194/tc-20-183-2026

Liston, G. E., Polashenski, C., Rösel, A., Itkin, P., King, J., Merkouriadi, I., & Haapala, J. (2018). A distributed snow-evolution model for sea-ice applications (SnowModel). *Journal of Geophysical Research: Oceans*, *123*(5), 3786–3810. https://doi.org/10.1002/2017jc013706

Liu, X. (2026). Python scripts, Jupyter notebooks, and results for "Systematic CRYO2ICE Snow-Thickness Retrieval over Antarctic Sea Ice Reveals Persistent Weddell-Ross Contrast Across Four Austral Winters". *Zenodo*. [software]. https://doi.org/10.5281/zenodo.19220192

Liu, X., Corney, S. P., Tilling, R. L., & Heil, P. (2025). Intercomparisons of Austral winter freeboards from satellite radar altimetry for Antarctic Sea Ice. *Authorea Preprints*.

Mallett, R., Nandan, V., Stroeve, J., Willatt, R., Saha, M., Yackel, J., et al. (2024). Dye tracing of upward brine migration in snow. *Annals of Glaciology*, *65*, e26. https://doi.org/10.1017/aog.2024.27

Markus, T., & Cavalieri, D. J. (1998). Snow depth distribution over sea ice in the Southern Ocean from satellite passive microwave data. *Antarctic sea ice: physical processes, interactions and variability*, *74*, 19–39.

Markus, T., & Cavalieri, D. J. (2009). The AMSR-E NT2 sea ice concentration algorithm: Its basis and implementation. *Journal of The Remote Sensing Society of Japan*, *29*(1), 216–225.

Markus, T., Neumann, T., Martino, A., Abdalati, W., Brunt, K., Csatho, B., et al. (2017). The ice, cloud, and land elevation Satellite-2 (ICESat-2): Science requirements, concept, and implementation. *Remote sensing of environment*, *190*, 260–273. https://doi.org/10.1016/j.rse.2016.12.029

Massom, R. A., Eicken, H., Hass, C., Jeffries, M. O., Drinkwater, M. R., Sturm, M., et al. (2001). Snow on Antarctic sea ice. *Reviews of Geophysics*, *39*(3), 413–445. https://doi.org/10.1029/2000rg000085

Meier, W. N., Markus, T., & Comiso, J. C. (2018). AMSR-E/AMSR2 unified L3 daily 12.5 km brightness temperatures, sea ice concentration, motion & snow depth polar grids (AU_SI12, version 1). *NASA National Snow and Ice Data Center Distributed Active Archive Center*. [dataset]. https://doi.org/10.5067/RA1MIJOYPK3P

Melsheimer, C., Spreen, G., Ye, Y., & Shokr, M. (2023). First results of Antarctic sea ice type retrieval from active and passive microwave remote sensing data. *The Cryosphere*, *17*(1), 105–126. https://doi.org/10.5194/tc-17-105-2023

Mitchell, J., Dzerdzeevskii, B., Flohn, H., Hofmeyr, W., Lamb, H., Rao, K., & Wallén, C. (1966). *Climatic change*. Technical Note, No. 79. (Vol. 99). World Meteorological Organization.

Moon, W., Nandan, V., Scharien, R. K., Wilkinson, J., Yackel, J. J., Barrett, A., et al. (2019). Physical length scales of wind-blown snow redistribution and accumulation on relatively smooth Arctic first-year sea ice. *Environmental Research Letters*, *14*(10), 104003. https://doi.org/10.1088/1748-9326/ab3b8d

Nab, C., Mallett, R., Nelson, C., Stroeve, J., & Tsamados, M. (2024). Optimising interannual sea ice thickness variability retrieved from CryoSat-2. *Geophysical Research Letters*, *51*(21), e2024GL111071. https://doi.org/10.1029/2024gl111071

Nandan, V., Geldsetzer, T., Yackel, J., Mahmud, M., Scharien, R., Howell, S., et al. (2017). Effect of snow salinity on CryoSat-2 Arctic first-year sea ice freeboard measurements. *Geophysical Research Letters*, *44*(20), 10–419. https://doi.org/10.1002/2017gl074506

Neumann, T. A., Martino, A. J., Markus, T., Bae, S., Bock, M. R., Brenner, A. C., et al. (2019). The ice, cloud, and land elevation Satellite–2 mission: A global geolocated photon product derived from the advanced topographic laser altimeter system. *Remote sensing of environment*, *233*, 111325. https://doi.org/10.1016/j.rse.2019.111325

Parkinson, C. L. (2019). A 40-y record reveals gradual Antarctic sea ice increases followed by decreases at rates far exceeding the rates seen in the Arctic. *Proceedings of the National Academy of Sciences*, *116*(29), 14414–14423. https://doi.org/10.1073/pnas.1906556116

Parkinson, C. L., & DiGirolamo, N. E. (2021). Sea ice extents continue to set new records: Arctic, Antarctic, and global results. *Remote Sensing of Environment*, *267*, 112753. https://doi.org/10.1016/j.rse.2021.112753

Rostosky, P., Spreen, G., Farrell, S. L., Frost, T., Heygster, G., & Melsheimer, C. (2018). Snow depth retrieval on Arctic sea ice from passive microwave radiometers—Improvements and extensions to multiyear ice using lower frequencies. *Journal of Geophysical Research: Oceans*, *123*(10), 7120–7138. https://doi.org/10.1029/2018jc014028

Saha, M., Stroeve, J., Isleifson, D., Yackel, J., Nandan, V., Landy, J. C., & Lam, H. M. (2025). Snow depth estimation on leadless landfast ice using CRYO2ICE satellite observations. *The Cryosphere*, *19*(1), 325–346. https://doi.org/10.5194/tc-19-325-2025

Sturm, M., & Massom, R. A. (2017). Snow in the sea ice system: Friend or foe? Sea ice (pp. 65–109).

Taelman, C., Landy, J., Mallett, R., & Itkin, P. (2026). Empirical evidence of overestimated Ku-band sea ice radar freeboards in satellite altimetry. *EGUsphere*, *2026*, 1–46. [preprint]. https://doi.org/10.5194/egusphere-2026-1662

Tian, T. R., Fraser, A. D., Lavergne, T., Fiddes, S. L., Zhao, C., & Heil, P. (2023). Linking timescale-dependent Antarctic sea ice kinematic observations to ice thickness. *Remote Sensing of Environment*, *298*, 113813. https://doi.org/10.1016/j.rse.2023.113813

Tison, J.-L., Maksym, T., Fraser, A. D., Corkill, M., Kimura, N., Nosaka, Y., et al. (2020). Physical and biological properties of early winter Antarctic sea ice in the Ross Sea. *Annals of Glaciology*, *61*(83), 241–259. https://doi.org/10.1017/aog.2020.43

Tiuri, M., Sihvola, A., Nyfors, E., & Hallikaiken, M. (1984). The complex dielectric constant of snow at microwave frequencies. *IEEE Journal of Oceanic Engineering*, *9*(5), 377–382. https://doi.org/10.1109/joe.1984.1145645

Turner, J., Phillips, T., Marshall, G. J., Hosking, J. S., Pope, J. O., Bracegirdle, T. J., & Deb, P. (2017). Unprecedented springtime retreat of Antarctic sea ice in 2016. *Geophysical Research Letters*, *44*(13), 6868–6875. https://doi.org/10.1002/2017gl073656

Ulaby, F. T., Moore, R. K., & Fung, A. K. (1986). Microwave remote sensing: Active and passive. volume 3-from theory to applications.

Warren, S. G., Rigor, I. G., Untersteiner, N., Radionov, V. F., Bryazgin, N. N., Aleksandrov, Y. I., & Colony, R. (1999). Snow depth on Arctic sea ice. *Journal of Climate*, *12*(6), 1814–1829. https://doi.org/10.1175/1520-0442(1999)012<1814:sdoasi>2.0.co;2

Webster, M., Gerland, S., Holland, M., Hunke, E., Kwok, R., Lecomte, O., et al. (2018). Snow in the changing sea-ice systems. *Nature Climate Change*, *8*(11), 946–953. https://doi.org/10.1038/s41558-018-0286-7

Willatt, R., Mallett, R., Stroeve, J., Wilkinson, J., Nandan, V., & Newman, T. (2025). Ku-and Ka-band polarimetric radar waveforms and snow depth estimation over multi-year Antarctic sea ice in the Weddell Sea. *Geophysical Research Letters*, *52*(13), e2024GL112870. https://doi.org/10.1029/2024gl112870

Willatt, R., Stroeve, J. C., Nandan, V., Newman, T., Mallett, R., Hendricks, S., et al. (2023). Retrieval of snow depth on Arctic sea ice from surface-based, polarimetric, dual-frequency radar altimetry. *Geophysical Research Letters*, *50*(20), e2023GL104461. https://doi.org/10.1029/2023gl104461

Williams, G., Maksym, T., Wilkinson, J., Kunz, C., Murphy, C., Kimball, P., & Singh, H. (2015). Thick and deformed Antarctic sea ice mapped with autonomous underwater vehicles. *Nature Geoscience*, *8*(1), 61–67. https://doi.org/10.1038/ngeo2299

Wingham, D., Francis, C., Baker, S., Bouzinac, C., Brockley, D., Cullen, R., et al. (2006). CryoSat: A mission to determine the fluctuations in Earth's land and marine ice fields. *Advances in Space Research*, *37*(4), 841–871. https://doi.org/10.1016/j.asr.2005.07.027

Worby, A., Geiger, C., Paget, M., Van Woert, M., Ackley, S., & DeLiberty, T. (2008). Thickness distribution of Antarctic sea ice. *Journal of Geophysical Research*, *113*(C5). https://doi.org/10.1029/2007jc004254

Worby, A., Markus, T., Steer, A. D., Lytle, V. I., & Massom, R. A. (2008). Evaluation of AMSR-E snow depth product over East Antarctic sea ice using in situ measurements and aerial photography. *Journal of Geophysical Research*, *113*(C5). https://doi.org/10.1029/2007jc004181

Zhou, L., Skourup, H., Stroeve, J., Kacimi, S., Arndt, S., Zhu, W., et al. (2026a). Snow effects on altimeter waveforms over sea ice in the Weddell Sea-Part II: Sea ice and snow spaceborne retrieval. *Remote Sensing of Environment*, *338*, 115360. https://doi.org/10.1016/j.rse.2026.115360

Zhou, L., Skourup, H., Stroeve, J., Kacimi, S., Arndt, S., Zhu, W., et al. (2026b). Snow effects on altimeter waveforms over sea ice in the Weddell Sea—Part I: Radar waveform decomposition. *Remote Sensing of Environment*, *333*, 115112. https://doi.org/10.1016/j.rse.2025.115112